11-29-2016

Large Scale Screening of Low Cost Ferritic Steel Designs For Advanced Ultra Supercritical Boiler Using First Principles Methods

Lizhi Ouyang
Tennessee State University

" LARGE SCALE SCREENING OF LOW COST FERRITIC STEEL DESIGNS FOR ADVANCED ULTRA SUPERCRITICAL BOILER USING FIRST PRINCIPLES METHODS"

FINAL SCIENTIFIC/TECHNICAL REPORT

Reporting Period July 1, 2013 through August 30, 2016

Lizhi Ouyang

November 29, 2016

DOE Award Number: DE-FE0011549

Principle Investigator: Lizhi Ouyang
Tennessee State University
3500 John A. Merritt Blvd.
Nashville, Tennessee 37209

DISCLAMER

ABSTRACT

Advanced Ultra Supercritical Boiler (AUSC) requires materials that can operate in corrosive environment at temperature and pressure as high as 760˚C (or 1400˚F) and 5000psi, respectively, while at the same time maintain good ductility at low temperature. We develop automated simulation software tools to enable fast large scale screening studies of candidate designs. While direct evaluation of creep rupture strength and ductility are currently not feasible, properties such as energy, elastic constants, surface energy, interface energy, and stack fault energy can be used to assess their relative ductility and creeping strength. We implemented software to automate the complex calculations to minimize human inputs in the tedious screening studies which involve model structures generation, settings for first principles calculations, results analysis and reporting. The software developed in the project and library of computed mechanical properties of phases found in ferritic steels, many are complex solid solutions estimated for the first time, will certainly help the development of low cost ferritic steel for AUSC.

Table of Contents

I.EXECUTIVE SUMMARY

This report summarizes our method development, software implementation, infrastructure improvement and computational studies for the ferritic steels during the three-year period.

- Calculations of all known phases found in ferritic steels of which majorities are solid solution phases. Many solid solution phases were for the first time systematically studied using first principles methods;
- Assessment of the zero temperature elastic properties of known 9-12Cr ferritic steels using Eshelby's inclusion theory for multiphase multicomponent system. The shear/bulk modulus ratio are used to indicate the ductility of the ferritic steel;

Additional modules for physical properties calculations are also developed:

- Development of G(p,T) module that automates the solid solution modeling based on structure template and composition parameters;
- Development of G(p,T) module that automate the physical properties calculations using special quasirandom structure methods;

To facilitate our software development, we had upgraded our computer cluster to a 36-node computer cluster (gpt.tsuniv.edu) using Intel Xeon server chips with 4GB RAM per core. We had involved three undergraduates and two master graduate students in this projects. One graduate student's thesis work was to develop a searchable database for crystal structure data mining.

II.INTRODUCTION

Background

Advanced ultra supercritical boiler (AUSC) targeted at operational temperature up to 760˚C and pressure up to 35MPa has so far disqualified all tested low cost ferritic steels as high temperature structural material [1-2]. Recent developed 9-12Cr steel such as T/P91 and T/P92 showed excellent short-term creep strength but suffered from sigmoidal creep behavior in long-term creep test. The cause of such behaviors had been revealed as the precipitation of complex Z-phase nitrides at the expense of nanoscale MX carbonitrides dispersed in the matrix [3]. MX carbonitrdes hinder the motion of dislocation and are responsible for the ferritic alloy's improved creep strength. The coarsening of $M_{23}C_6$ particles which reside primarily at the grain boundaries also contribute to the loss of long term creep strength. Abe *et al* had demonstrated that the carbon and nitrogen concentrations affect the evolution of MX carbonitrides and boron stabilizes $M_{23}C_6$ particles [4].

To meet the requirements of AUSC, besides sufficient creeping strength at high temperature and pressure, new ferritic steels must also have excellent oxidation resistance and sufficient low temperature ductility. Among ferritic steels studied, steel contains 9-12% Cr shows excellent oxidation resistance by forming a dense oxide film that prevents the propagation of corrosion. Tempering at elevated temperature improves low temperature ductility. In the past few decades, tremendous efforts had devoted to control microstructure evolution at high temperature by modifying precipitation structure and composition. The key issues in searching for ferrite steel for AUSC are thus to understand the relation of structure and mechanical properties and control the precipitation microstructure and composition.

As the matrix phase of the 9-12Cr ferritic steel, the composition effects on its mechanical properties have been extended studied by many research teams. Leslie et al summarized the effect of alloying elements on the mechanical properties of BCC phase [5]. Cr shows an exceptional behavior that the strengthen effect increase with decreased temperature up to room temperature and drop sharply to softening at about 150K. Al has the most significant embrittlement effect on the BCC solid solution by promoting phase transition to intermetallic phase and grain boundary segregation. Simple models were used by the author to rationale the observed composition effect on mechanical properties. However our understanding of the mechanisms for the observed is unsatisfactory as these models succeed in some cases while fail in other cases.

In this project, we focus on develop large scale screening approaches based on physical properties of phases found in 9-12Cr ferritic steel. The goal of this project is two-fold: (1) to extend a solid solution modeling module to handle larger number of elements, to implement fast algorithms such as special quasirandom structure (SQS) method [6] for physical properties calculation of solid solution, to develop modules to calculate additional properties need to assess ductility; (2) to calculate the elastic properties of the solid solutions for given composition sampling. The results are used to construct the database for likelihood analysis which can be used to identify composition of new ferritic steel that are likely to succeed in quest for high temperature application in AUSC.

G(P,T) Package for Thermodynamic and Mechanical Properties Calculations

Our in-house developed G(P,T) package [7] has been successfully applied to calculate thermodynamic properties and mechanical properties of various ceramics and metals [8]. With support from NETL, we have extended our in-house Gibbs free energy package G(P,T) based on

first principles density functional theory for assessment thermodynamic and mechanical properties of solid solution and automation of large scale screening calculations. The G(P,T) package which is capable of computing physical properties of crystals such as elastic tensor, phonon structure, Helmoltz and Gibbs free energy and many other thermodynamic properties such as entropy, heat capacity, isothermal bulk modulus, thermal expansion coefficient, and Grüneisen parameters, *etc*. G(P,T) use the Vienna ab initio package (VASP) [9] for electronic structure, force and ground state energy calculations. The G(P,T) package has been designed to run efficiently on parallel computing architecture and has already been deployed on supercomputers of NERSC and ORNL. In its current implementation, G(P,T) package has shown to be scalable to at least thousands of processors in our recent phonon calculation of a 220-atom Al_2O_3 grain boundary model.

Solid Solution Modeling

Solid solution modeling using first principles method can be very challenging. The current state-of-the-art method can only scale up to about 1000 transitional metal atoms. In practice, we often limited the periodic structure unitcell to be less than 200 atoms, which can take a few hours for a self-consistent calculation on a small cluster. For large scale screening where large number of such calculations are needed, we will have to limit our models to be less than 200 atoms per unitcell. While other methods such as coherent potential method are frequently cited in the literature, we limit our discussion to methods based on VASP since we need to compare over many phases which has been calculated and validated using VASP. Cluster expansion method is a rigorous approach to compute solid solution properties. However, it is computationally extremely expensive, especially for multi-lattice multi-component system. We have implemented in G(p,T) the unitcell expand method. To reduce computation time, the special quasirandom

structure (SQS) method, which assume structure complies to high temperature limit of cluster expansion, can be used to estimate solid solution properties. Instead of calculate a large series of models to construct the cluster expansion, only a few structure models are needed for SQS. There models have cluster distribution functions matches those of the high temperature limit within a cutoff range. We used the mcsqs program included in the ATAT package to generate SQS models.

Unitcell Expansion Method

For multicomponent multisublattice solid solution, we had implemented a coarse grained cluster expansion method, the unitcell expansion method (UEM), in the G(p,T) package. In traditional cluster expansion method, the energy was expressed in terms of atomic clusters. In practices, a maximum complete cluster set γ is used as cut off in the energy expression,

$$E(\vec{\sigma}) \cong \sum_{\alpha \in \gamma} V_{\alpha} \Phi_{\alpha}(\vec{\sigma}) \qquad (1)$$

where $\vec{\sigma} = \langle \sigma_1, \sigma_2, \cdots, \sigma_N \rangle$ is the configuration vector, α is a cluster in γ, σ_i is the site occupation variable at *i*th lattice site, V_α is the effective cluster interaction coefficient, and $\Phi_\alpha(\vec{\sigma})$ is the cluster function of cluster α. The above approach has been extensive used to study binary alloys. However, if the lattice is complex and many non-equivalent lattice sites existed in the structure, the traditional cluster expansion method can be computationally expensive if not prohibitive. In the case of boron carbide, where carbon atoms could reside randomly on the stable conjugated icosahedra, the maximum cluster can be exceedingly large as huge maximum cluster set with clusters up to 12 atoms may be needed. the energy of the disordered crystal in terms of primitive unitcell,

$$E(\vec{\eta}) \cong \sum_{\beta \in \varsigma} V_{\beta} \Phi_{\beta}(\vec{\eta}) \qquad (2)$$

where ζ is the maximum complete cluster set of unitcells, β is a cluster in ζ, $\vec{\eta} = \langle \tau_1, \tau_2, \cdots, \tau_L \rangle$ is the configuration vector, $\tau_i = \tau\left(\sigma_1^{(i)}, \sigma_2^{(i)}, \cdots, \sigma_{n_i}^{(i)}\right)$ is *i*th unitcell configuration variable, V_β is the effective unitcell cluster interaction coefficient, and $\Phi_\beta(\vec{\sigma})$ is the unitcell cluster function of cluster β. Energy expansion in terms of unitcells trades the complexity in lattice for increased component types. For one unique site simple lattice such as BCC/FCC, UEM reduces to traditional cluster expansion method. For complexity lattice, particularly large unitcells, UEM has significant advantages. First, it is possible to reduce the number of unique unitcell types, $\boldsymbol{n}_\tau$. For a given concentration, we can carry out an extensive in unitcell or small supercell calculations to identify the lowest configurations that will be used in the UEM calculations. Second, if the unitcell is large enough, it is possible only small clusters up to near-neighbor clusters or at most triplets will be needed in the energy expression, thus the total number of effective cluster interaction coefficients (ECI) $N_{\boldsymbol{\beta},\mathbf{n}_\tau}$, remains manageable (~$\boldsymbol{n}_\tau^{2\sim3}$). Third, it is quite simple to introduce lattice defects, surface structures in this approach. If only considering the nearest neighbor interaction, the UEM becomes a Potts model. Potts models is a generalized Ising model in which a finite set of symbols, here we referred as unique unitcell types, is used to defined to the lattice site occupations,

$$H_g = -\sum_{(i,j)} J_{ij}\boldsymbol{\delta}(\boldsymbol{\tau}_i, \boldsymbol{\tau}_j) - \sum_i h_i \boldsymbol{\tau}_i \qquad (3)$$

where J_{ij} is the near-neighbour interaction, h_i is the self-interaction energy coefficient of *i*th lattice site.

The UEM approach requires significant amount computational resource and is not suitable for large scale screening. Instead, we implemented the special quasirandom structure method (SQS), developed by Zunger *et al*, which requires only few supercell calculations to evaluate

properties of solid solution. In the SQS method, physical properties can be expressed ensemble average of configurations,

$$\langle P \rangle = \Sigma_{k,m} D_{k,m} \langle \Pi_{k,m} \rangle p_{k,m} \quad (4)$$

where $D_{k,m}$ are the number of figures per site, $p_{k,m}$ are the interaction parameters of figures (k,m) and $\Pi_{k,m}$ are the correlation function. Unlike cluster expansion method, the central idea of SQS is to estimate $\langle \Pi_{k,m} \rangle_R$ using statistical sampling method over a few specially design N-atom periodic structure S whose distinct correlation funtions $\Pi_{k,m}(S)$ best match $\langle \Pi_{k,m} \rangle_R$.

Temperature-Pressure Dependent Elastic Constants

The G(p,T) package also has the ability to computationally assess the high temperature mechanical properties. Considering a periodic cell under temperature *T*, a small external strain ε_{ij} is applied to the cell. With the G(P,T) package, we can calculate the Helmholtz free energy $F(T, \varepsilon_{ij})$ of the perturbed cell. Ignoring high order terms, the Helmholtz free energy $F(T, \varepsilon_{ij})$ of the cell can be expanded around the unstrained reference cell $\boldsymbol{0}$ as,

$$F(T, \varepsilon_{ij}) \approx F(T, \boldsymbol{0}) - \sigma_{ij}(T, \boldsymbol{0})\varepsilon_{ij} + \tfrac{1}{2} C_{ijkl}(T, \boldsymbol{0})\, \varepsilon_{ij}\, \varepsilon_{kl} \quad (5)$$

where $\sigma_{ij}(T, \boldsymbol{0})$ and $C_{ijkl}(T, \boldsymbol{0})$ are the temperature dependent stress tensor and elastic tensor of the reference cell, respectively. Helmholtz free energy $F(T, \varepsilon_{ij})$ has 7 independent variables: the second order strain tensor has up to 6 independent components and temperature. Sampling of $F(T, \varepsilon_{ij})$ in the 7-dimension space to calculate temperature elastic tensor of any reference cell would be computationally too costly. However, if we consider only reference cell under hydrostatic press *P*, we can significantly reduce the sampling to only 2 dimensions as the cell shape and size is uniquely determined by temperature *T* and hydrostatic pressure *P*. However, the cell shape and size are unknown for given *T* and *P*. Our approach is to sample around the zero temperature reference cell $\boldsymbol{0}$ under pressure *P* which is obtained from total energy relaxation.

Assuming at temperature T, the thermal stress leads to a strain ε^t_{ij}, equations (5) can then be rewritten as

$$F(T, \varepsilon_{ij}) \approx F(T, \mathbf{0}+\varepsilon^t_{ij}) - \sigma_{ij}(T, \mathbf{0}+\varepsilon^t_{ij})(\varepsilon_{ij}-\varepsilon^t_{ij}) + \tfrac{1}{2}C_{ijkl}(T, \mathbf{0}+\varepsilon^t_{ij})(\varepsilon_{ij}-\varepsilon^t_{ij})(\varepsilon_{kl}-\varepsilon^t_{kl}) \quad (6)$$

Let $\varepsilon'_{ij} = \varepsilon_{ij} - \varepsilon^t_{ij}$, $\mathbf{0}' = \mathbf{0} + \varepsilon^t_{ij}$, and $\sigma_{ij}(T, \mathbf{0}+\varepsilon^t_{ij}) = P\cdot\delta_{ij}$ where δ_{ij} is the Kronecker delta, we have,

$$F(T, \varepsilon_{ij}) \approx F(T, \mathbf{0}') - P\cdot\delta_{ij}(\varepsilon_{ij}-\varepsilon^t_{ij}) + \tfrac{1}{2}C_{ijkl}(T, \mathbf{0}')(\varepsilon_{ij}-\varepsilon^t_{ij})(\varepsilon_{kl}-\varepsilon^t_{kl}) \quad (7)$$

where $C_{ijkl}(T, \mathbf{0}')$ is the elastic tensor at temperature T and pressure P. The thermal stress induced strain can be estimated from equation (2), $\varepsilon^t_{ij} \approx S_{ijkl}(T,\mathbf{0})(\sigma_{kl}(T, \mathbf{0}) - P\cdot\delta_{kl})$. A simple linear regression model can be used to find the elastic tensor based on equation (6) and (7). Other properties such as thermal expansion tensor can also be calculated in similar way.

III. Methodology Development

A.1 G(P,T) module for automated structure modeler

We completed the implementation of a G(p,T) module to automate the proposed calculations. A set of scripts for input file preparation have been developed:

(1) *getnimscif*: a script to retrieve crystal structure data in CIF format from the NIMS database (http://crystdb.nims.go.jp/index_en.html)

(2) *gulp2xml*: convert simple GULP structure input file to xml prototype structure file. Example is shown in Appendix 1.

(3) *xml2gulp*: generate GULP input based the xml template. For example

- ~> xml2gulp –i czts.xml –s "Cu Fe Cr Se; .5 .5 0 0;0 .5 .5 0;.5 0 .5 0;0 0 0 1"

  The above command will substitute the Cu, Zn, Sn, S with ($Cu_{0.5}$ $Fe_{0.5}$), ($Fe_{0.5}$, $Cr_{0.5}$), ($Cr_{0.5}$ $Cu_{0.5}$) and Se.

(4) *xml2int*: generate internal input format used by G(p,T) package.

(5) *xml2mcsqs*: generate input file for *mcsqs* program which is part of the ATAT package. We are working on our own program to improve the convergence of the special quasi-random structure generation tool.

Steel has a very complex multiscale structure including many solid solution phases. To automate the calculation of these solid solution systems, we use the strategy that separates the lattice and basis from site occupation. Any atomic structure can be described by,

$$\mathbf{S} \rightarrow \{ \mathbf{R}_i; \mathbf{O}_i \} \tag{8}$$

where S represents the structure, $\mathbf{R}_i$ is the location of *i*th atomic site, and $\mathbf{O}_i$ is the occupation index at the *i*th atomic site. For crystal and solid solution,

$$\{\mathbf{R}_i\} = \{\underline{\mathbf{L}_j}\, r_k\} = \{\underline{\mathbf{L}_j}\} \otimes \{r_k\} \qquad i \rightarrow \{j, k\} \tag{9}$$

where all lattice sites can be generated by all translation of operators $\{\underline{\mathbf{L}_j}\}$ acting on the lattice basis $\{r_k\}$. The index *i* is uniquely mapped to the pair {j,k}. The set of occupation index $\{\mathbf{O}_i\}$, however, cannot be directly generated from $\{\underline{\mathbf{L}_j}\}$ acting on the corresponding occupation basis $\{o_i\}$ except perfect crystal with occupation periodicity. Introducing collapse operator $\underline{\mathbf{C}}$, inverse to $\underline{\mathbf{L}}$,

$$\{\langle r_{k,j} \rangle\} = \{\underline{\mathbf{C}_j}\, \mathbf{R}_{\{j,k\}}\} \tag{10}$$

where $\mathbf{q}_k = \langle r_{k,j} \rangle$ is a replica vector of r_k with index j, i.e. $\langle r_1, r_1, r_1, r_1, r_1, r_1 \ldots \rangle$. Similarly,

$$\{\langle o_{k,j} \rangle\} = \{\underline{\mathbf{C}_j}\, \mathbf{O}_{\{j,k\}}\} \tag{11}$$

where $\mathbf{p}_k = \langle o_{k,j} \rangle$ is a replica vector of o_k with index j, i.e. $\langle o_{1,1}, o_{1,2}, o_{1,3}, o_{1,4}, o_{1,5} \ldots \rangle$. At each position with index j, the occupation index can be different at each component in case of solid solution. Under translational operation, i.e., shifting the j index of the replica vector component, the replica vector for atomic position is invariant; the replica vector for occupation index is not. Of course, the total energy of the system is invariant under translational operation.

Let us take the P91 steel as an example. The follow structure facts, as shown in table 1, can be retrieved from various databased and literatures.

Tabel 1. Mole fraction of atoms in steel P91 and its phases at T=300K and P=1atm

Steel	Al	C	Cr	Fe	Mn	Mo	N	Nb	Ni	Si	V
P91	0.003	0.005	0.088	0.882	0.004	0.005	0.002	0.0004	0.001	0.007	0.002
A2-1	0.003		0.001	0.990						0.007	
A2-2			0.946		0.054						
C14			0.545		0.333					0.122	
Z			0.338	0.038			0.247				0.377
NbNi3								0.250	0.750		
AlN	0.500						0.500				
M23C6		0.207	0.685	0.005		0.103					

Clearly, there are only two crystal phases, $NbNi_3$ and AlN in P91 and the rest are solid solution phases. To generate structure model from the above table directly can be a great challenge, as the occupations of lattice basis cannot be directly obtain from those overall information, For example, for Z-phase, there could be many possible distributions on its 6 lattice basis that satisfy the mole fraction restrict from the table, N atoms can either occupy all 6 lattice basis at 24.7% probability or only 2 lattice basis at 86.1% probability.

It is possible to directly calculate the site occupation in the solid solution using cluster expansion approach but the computational cost can be prohibiting. Since the aim of this project is to screen large number of possible concentration, it is necessary to develop a much fast approach to estimate properties of the solid solution.

Examples

1. Sample xml template file, generated from czts.gin

==========

```
<?xml version="1.0" encoding="ISO-8859-1"?>
<struct_prototype>
  <i name="prototype_name">CZTS</i>
  <i name="prototype_comment">Cu-Zn-Sn-S compound for PV</i>
  <i name="prototype_SBS">CZTS</i>
```

```
<symmetry>
  <i name="space_group">121</i>
  <i name="space_group_pearson">tI16</i>
  <i name="space_group_point_group">D2d</i>
  <i name="space_group_hm">I-42M</i>
  <i name="origin">1</i>
</symmetry>
<cell>
  <v name="cell_free_parameters"> 5.435 10.843 </v>
  <v name="cell_parameters"> 5.435 5.435 10.843 90 90 90 </v>
  <varray name="uc_vectors">
    <v name="uc_a">       5.4350000       0.0000000       0.0000000 </v>
    <v name="uc_b">       0.0000000       5.4350000       0.0000000 </v>
    <v name="uc_c">       0.0000000       0.0000000      10.8430000 </v>
  </varray>
  <varray name="pc_vectors">
    <v name="pc_a">      -0.5000000       0.5000000       0.5000000 </v>
    <v name="pc_b">       0.5000000      -0.5000000       0.5000000 </v>
    <v name="pc_c">       0.5000000       0.5000000      -0.5000000 </v>
  </varray>
</cell>
<composition>
  <i name="number_of_elements"> 4 </i>
  <v name="elements"> Cu Zn Sn S  </v>
  <i name="number_of_composition_vectors"> 4 </i>
  <varray name="composition_vectors">
    <r id="1"> 1  0  0  0 </r>
    <r id="2"> 0  1  0  0 </r>
    <r id="3"> 0  0  1  0 </r>
    <r id="4"> 0  0  0  1 </r>
  </varray>
</composition>
<lattice_basis>
  <i name="number_of_wyckoff_sites"> 4 </i>
  <i name="number_of_sites_uc"> 16 </i>
  <set name="site_list_uc">
    <r id="1" idirr="1" wyckoff="d" multi="4" idaw="1" >   0.000000   0.500000   0.250000 </r>
    <r id="2" idirr="1" wyckoff="d" multi="4" idaw="2" >   0.500000   0.000000   0.750000 </r>
    <r id="3" idirr="1" wyckoff="d" multi="4" idaw="3" >   0.500000   0.000000   0.250000 </r>
    <r id="4" idirr="1" wyckoff="d" multi="4" idaw="4" >   0.000000   0.500000   0.750000 </r>
    <r id="5" idirr="2" wyckoff="a" multi="2" idaw="1" >   0.000000   0.000000   0.000000 </r>
    <r id="6" idirr="2" wyckoff="a" multi="2" idaw="2" >   0.500000   0.500000   0.500000 </r>
    <r id="7" idirr="3" wyckoff="b" multi="2" idaw="1" >   0.000000   0.000000   0.500000 </r>
    <r id="8" idirr="3" wyckoff="b" multi="2" idaw="2" >   0.500000   0.500000   0.000000 </r>
    <r id="9" idirr="4" wyckoff="i" multi="8" idaw="1" >   0.244900   0.244900   0.129800 </r>
    <r id="10" idirr="4" wyckoff="i" multi="8" idaw="2" >   0.744900   0.744900   0.629800 </r>
    <r id="11" idirr="4" wyckoff="i" multi="8" idaw="3" >   0.255100   0.255100   0.629800 </r>
    <r id="12" idirr="4" wyckoff="i" multi="8" idaw="4" >   0.755100   0.755100   0.129800 </r>
    <r id="13" idirr="4" wyckoff="i" multi="8" idaw="5" >   0.744900   0.255100   0.370200 </r>
    <r id="14" idirr="4" wyckoff="i" multi="8" idaw="6" >   0.244900   0.755100   0.870200 </r>
    <r id="15" idirr="4" wyckoff="i" multi="8" idaw="7" >   0.255100   0.744900   0.370200 </r>
    <r id="16" idirr="4" wyckoff="i" multi="8" idaw="8" >   0.755100   0.244900   0.870200 </r>
  </set>
  <i name="number_of_sites_pc"> 8 </i>
  <set name="site_list_pc">
    <r id="1" idirr="1" wyckoff="d" multi="4" idaw="1" >   0.750000   0.250000   0.500000 </r>
```

```
    <r id="2" idirr="1" wyckoff="d" multi="4" idaw="2" >   0.250000   0.750000   0.500000 </r>
    <r id="3" idirr="2" wyckoff="a" multi="2" idaw="1" >   0.000000   0.000000   0.000000 </r>
    <r id="4" idirr="3" wyckoff="b" multi="2" idaw="1" >   0.500000   0.500000   0.000000 </r>
    <r id="5" idirr="4" wyckoff="i" multi="8" idaw="1" >   0.374700   0.374700   0.489800 </r>
    <r id="6" idirr="4" wyckoff="i" multi="8" idaw="2" >   0.884900   0.884900   0.510200 </r>
    <r id="7" idirr="4" wyckoff="i" multi="8" idaw="3" >   0.625300   0.115100   0.000000 </r>
    <r id="8" idirr="4" wyckoff="i" multi="8" idaw="4" >   0.115100   0.625300   0.000000 </r>
   </set>
   <set name="site_occupancy_list">
    <i idirr="1"> 1 </i>
    <i idirr="2"> 2 </i>
    <i idirr="3"> 3 </i>
    <i idirr="4"> 4 </i>
   </set>
  </lattice_basis>
</struct_prototype>
```

The GULP input file:

```
single verb full nosymm
title
prototype_name      CZTS
prototype_comment   Cu-Zn-Sn-S compound for PV
prototype_SBS       CZTS
spacegroup_pearson  tI16
end title
cell
5.435 5.435 10.843 90 90 90
frac
Cu1   core   0  1/2  1/4          # 4 d
Zn1   core   0  0    0            # 2 a
Sn1   core   0  0    1/2          # 2 b
S1    core   0.2449 0.2449 0.1298  # 8 i
space
121
dump czts-uc.gin
```

.

A.2 G(P,T) module implementing the special quasirandom structures method

The goal of this task is to implement the special quasirandom structures method to speed up the calculation of properties of solid solution at the price of acceptable loss of accuracy. The module is responsible to invoke structure modeler implemented in A.1 to produce the set the special structures and setup VASP calculations to obtain properties of the set. The results of these calculations can then to obtain solid solution properties through ensemble average.

A set of scripts have been developed to automate the generation of the special quasirandom structure using structure prototype and chemical composition. The composition determined from experiment requires huge number of atoms to match exactly which is not possible with first principles methods. To limit the size of model, we limited the minimal concentration of elements to be greater than 0.2% and the concentration has to be rounded to ensure integer number of atoms in the SQS model.

(1) mcsqs2int: the script runs a Monte Carlo simulation to generate SQS structure and convert the output to internal format of the G(p,T) package

(2) mcsqs2aims: the script convert the output from SQS calculation to input files for FHI-Aims program, a numeric LCAO based method we purchased.

Eshelby Inclusion Theory for Homogenization of Multiphase Composite Materials

Mechanical properties of ferritic steels depend on their multiscale structure. Direct simulation of the complex multiscale structure from atomistic steel is computational prohibitive. Eshelby inclusion theory (J. D. Eshelby, Elastic Inclusions and Inhomogeneities, in Progress in Solid Mechanics,2nd ed. IN. Sneddon and R. Hill, North-Holland, Amsterdam, 1961. pp. 89-140.) provides a homogenization scheme to estimate ferritic steel elastic properties from elastic properties of each phases found in the steel and volume composition and grain size distribution. Since all precipitation phases form smaller particles comparing to the matrix BCC iron phase, it is reasonable to assume all inclusion, or precipitating, particles are in ellipsoidal shape.

Based on the Eshelby's elliptical inclusion theory, we implemented an iteration scheme to compute the homogenized elastic properties of ferritic steels based on volume partition and elastic properties of all phases involved. The Effective Self Consistent Scheme (ESCS) for homogenization is described as,

$$C^* = (H + C_M^{-1})^{-1} \quad (12)$$

where C^* is the homogenized elastic tensor, C_M is the elastic tensor of the matrix phase, and H is the compliance increment which is to be obtained through the following implicit relation,

$$H = \text{sum}\ (H_{I,i}^{d}\ (I - \Omega_{DI,i}\ H)^{-1} \quad (13)$$

where $\Omega_{DI,i}$ are the eigenstiffness of the *i*th inclusion phase, $H_{I,i}^{d}$ is the dilute limit estimation of the *i*th inclusion phase, which both can be estimated based on Eshelby's theory,

$$H_{I,i}^{d} = c_i\ \{\ (C_{I,i}^{-1} - C_M^{-1})^{-1} + C_M(I - S_{I,i}^{M})\ \}^{-1} \quad (14)$$

$$\Omega_{DI,i} = C^*(I - S_{I,i}^{*}) \quad (15)$$

where $S_{I,i}^{M}$ is the Eshelby tensor for the *i*th inclusion phase in matrix phase, c_i is the volume fraction of the *i*th inclusion phase, and $C_{I,i}$ is the *i*th inclusion phase elastic tensor, $S_{I,i}^{*}$ is the Eshelby tensor for the *i*th inclusion phase in unknown effective medium.

The above scheme was programmed in python script named *homogenize*. In our implementation, H is initialized to zero. C* is then calculated to the estimation of $S_{I,i}^{*}$, which is then used to estimate a new H. The process repeated until the difference in H is less than certain convergence criteria.

IV. Results and Discussions

We use the following accuracy setting for all VASP calculations: (1) planewave energy cutoff is 400eV; (2) energy convergence is 10^{-8}eV/cell and force convergence is 10^{-5}eV/Å; (3) use reciprocal mesh for charge density representation.

Application to 9-12Cr Ferritic Steels

B.1 Properties of known 9-12Cr ferritic steel

Our goal is to search for low cost ferritic steel that can be used in next generation AUSC boiler. AUSC boiler requires material properties that are not met satisfactorily by available ferritic steels. Properties such as high temperature creeping strength, oxidation resistance, and low temperature ductility are critical to the success of AUSC boiler. Accurate direct assessment of these properties of a given ferritic steel composition using first principles based method is currently infeasible since steels have a complex structure whose properties are greatly affected not just by the atomic structure of phases presented but also the microstructure of grains and precipitations whose formation is driven by both thermodynamics and material processing. Instead, we aim here to screen ferritic steel alloys that will meet the material properties requirements, in this project, low temperature ductility, that can be reasonable estimated using first principles methods without much experimental inputs.

Ductility of alloy can be assessed using Poisson's ratio or more sophisticated, the Rice-Thompson parameter. For steel, calculating these parameters is a non-trivial task. In the case of AXM steel, it has 11 phases presented. Among the 11 phases, 9 are solid solution phases. To make the calculations computationally feasible, we used the special quasi-random structure methods to model the solid solutions. To estimate the overall mechanical properties of steels from the properties of phases presented, we used the method based on Eshelby's inclusion theory for homogenization in which the effect of microstructure can be estimated based on phase volume composition assuming certain microstructure morphology.

Figure 1 illustrates the screening process. Alloy compositions and phase compositions are the input of the screening process. First phases properties are calculated using first principles method.

Next homogenization method is used to calculate overall properties. The result is used to help searching for compositions that have desired properties

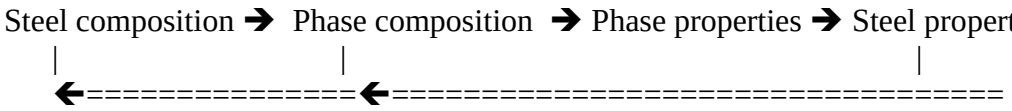

Figure 1. Feedback loop of the screening process.

Composition and Phases of known 9-12Cr Ferritic Steels

There are 12 known 9-12Cr ferritic steels included in present study: P91, P92, E911, AXM, HCM12, P122, T122, NF12, FN5, TB12, VM12, and X20. The dominant phase (>80%) is the body centered cubic (BBC) iron phase of A2 (Strukturbericht symbol). These BCC-A2 iron solid solution phases have less than 4% other dopants. Limited by computational power, only elements with over 0.2% are included in the solid solution models. Exactly matching the experimentally determined composition is not possible with a model of less than 200 atoms. Instead, a linear interpolation scheme to estimate its properties is used by computing models with compositions slightly off the experimental determined values as permitted by model size. For example, $Fe_{0.964}Si_{0.036}$ is to be estimated from $Fe_{96}Si_4$ and $Fe_{97}Si_3$ solid solution models.

Table 2 lists all matrix phase computed. Assuming power law holds for doping concentration dependent elastic modulus ($\Delta\tau \sim c^{1/2}$).

Table 2. computed elastic properties of Iron matrix phase (unit: GPa)

Steel	Composition	K	G	E	ν
P91	[Fe0.9898Si0.0066Al0.0028X]	228	82	219	0.340
E911	[Fe0.9969Si0.0020X]	210	95	247	0.304
P92	[Fe0.9944Si0.0038Al0.0006X]	219	89	234	0.322
AXM	[Fe0.9964Si0.0013Al0.0012X]	218	76	205	0.343
X20	[Fe0.9938Si0.0044X]	212	101	262	0.295
VM12	[Fe0.9704Co0.0174Si0.0111X]	248	73	200	0.366

HCM12	[Fe0.9977Si0.0017X]	210	94	244	0.306
NF12	[Fe0.9650Co0.0282Si0.0060X]	208	85	245	0.320
P112	[Fe0.9986X]	204	81	215	0.325
FN5	[Fe0.9677Co0.0303Si0.0012X]	208	85	224	0.320
T112	[Fe0.9929Si0.0059X]	214	104	269	0.290
TB12	[Fe0.9990X]	204	81	215	0.325

Summarized in Table 3 are the precipitation phases in 9-12Cr ferritic steels. There are total 14 lattice prototypes found in the 12 known ferritic steels we studied. Most of the well- known 9-12Cr ferritic steels contain over seven elements and over six precipitate phases of different volume fractions. The microstructure of ferritic steels contains the nanometer scale and micrometer scale precipitating particles presented inside the matrix phase, grain boundaries, and multi-grain pocket areas.

The volume fractions of precipitate phases in each steel phase studied here are presented in figure 2. In the figure, y-axis represent for the cumulative volume fraction and x-axis steel phase type. Height of the shade (color) in the figure shows the proportional volume fraction of the precipitate phase in the steel phase.

Most of the precipitate phases consist of many elements in it in different ratio. In actual structure, there could be some elements in very small concentration. To model the structures containing very small concentration of elements, the model structure need to be very large (thousands of atoms) and this is not possible in ab initio simulation yet. Similar to the practice used for matrix phase, we only include the elements with relatively larger concentration in the structure models. And, an interpolation scheme is used to estimate the properties of the precipitation phases.

Table 3. Precipitating phases in known 9-12Cr ferritic steels. PT and SG are abbreviations for structure prototype and space group, respectively.

			Steel Phases											
Precipitate Phase	PT	SG	P91	P92	E911	AXM	HCM 12	P122	T122	NF12	FN5	TB12	VM1 2	X20
BCC_A2	W	229	x	x	x	x	x	x	x	x	x	x	x	x
M23C6	Mn23Th6	225	x	x	x	x	x	x	x	x	x	x	x	x
LAVES	MgZn2	194	x	x	x		x	x	x	x	x	x	x	x
Z_PHASE	NaCl	225	x	x	x	x	x	x	x	x	x	x	x	x
NBNI3	Al3Ti	139	x			x	x	x	x	x	x			
ALN	NiAs	194	x	x	x	x		x	x			x		
SIGMA	CrFe	136		x	x							x		
FCC_A1	Cu	225		x	x	x	x	x	x	x		x	x	x
HCP_A3	Mg	194			x							x		
M2B_TETR	Fe2B	140		x		x								
MU_PHASE	W6Fe7	166				x								
M6C	W3Fe3C	227				x								
CR2B_ORT	Mg2Cu	70						x	x	x	x		x	
PI	Mo3Al2C	70										x	x	

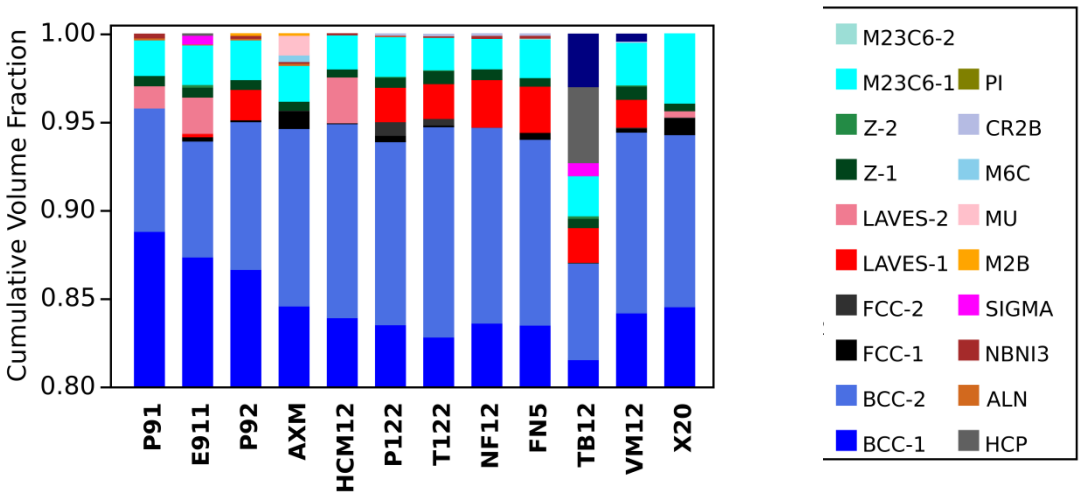

Figure 3. Volume fraction of precipitate phases in steel phases. Height of the color band represent volume fraction of precipitate phase (color band) in steel phase.

Computational Methods

We used special quasirandom structure method to generate initial structures for each precipitate phase containing fractional atomic positions. The models obtained from the mcsqs

were then fully relaxed (allowing to change both volume, cell shape and atomic positions sufficiently well) using Vienna ab-initio simulation package (VASP). VASP is a density functional theory based method. It is very accurate and efficient for geometry optimization, stress and force related calculations. As we have many large models we used gamma only calculation with PAW_PBE exchange correlation functional. Sufficiently relaxed models were then used for elastic properties calculations. For elastic properties calculations, we used the elastic module implemented in the G(p,T) package. In this approach, we applied a set of small strains at a step size of 0.01 in each independent strain element and the ions in the structure were relaxed keeping the volume and shape of the structure fixed. After sufficient relaxation ions, stress tensor was calculated. From the set of strain and stress data, elastic stiffness constants were calculated according to the tonsorial form of Hook's law. From the calculated elastic tensor, we estimated the polycrystal bulk properties using Voight-Reuss-Hill (VRH) approximation.

Results and Discussions

The calculated elastic constants C_{ij} (GPa) of steel precipitate phases are presented in table 3. The bulk modulus, shear modulus, Young's modulus, and Poisson's ratio are calculated from elastic constants using the VRH approximation. We noticed that, even though the composition varied significantly for some solid solution precipitation phases including the $M_{23}C_6$, Laves phase, and Z-phase, their elastic constants appear to be very stable and not vary accordingly. For example, the C_{ij} of precipitate phases $M_{23}C_6$ and Laves phases are large and similar in all steel phases. Note that all models used in present study contain no vacancy and interstitial defects. Elastic constants of most solid phases in present study are estimated for the first time and we have little experimental data to compare with.

Table 4. Summary of computed elastic constants and mechanical properties of phases found in the 9-12Cr ferritic steels. K, G, E and **η** represent bulk modulus, shear modulus, E Young's modulus and Poisson's ratio, respectively. All the data in table are in GPa.

AXM

Phase	C_{11}	C_{33}	C_{44}	C_{66}	C_{12}	C_{13}	K	G	E	η
BCC_A2-1	376.3	432.9	42.4	72.7	232.1	135.4	238.9	67.4	184.8	0.371
BCC_A2-2	396.4	396.4	125.6	125.6	215.0	215.0	275.5	110.2	291.8	0.324
FCC_A1-1	311.8	343.2	146.3	147.9	205.4	165.6	224.8	106.3	275.4	0.296
FCC_A1-3	180.3	180.4	82.7	82.7	120.8	120.8	138.9	54.9	145.5	0.325
ALN	377.4	356.1	113.5	125.6	128.8	98.9	195.7	122.5	304.0	0.241
M23C6	459.0	459.0	111.3	111.5	216.1	216.1	297.1	115.2	306.1	0.328
Z_PHASE	278.3	250.4	44.9	7.9	182.7	172.8	189.2	29.1	83.0	0.427
NBNI3	290.2	305.9	113.3	111.4	178.2	152.7	205.6	90.9	237.7	0.307
M2B_TETR	439.8	504.1	141.7	135.6	199.5	190.1	282.1	137.0	353.6	0.291
MU_PHASE	433.6	405.8	93.0	93.6	245.0	219.2	292.7	94.6	256.1	0.354
M6C	441.5	441.5	114.9	114.9	202.6	202.6	282.2	116.6	307.6	0.318

E911

Phase	C_{11}	C_{33}	C_{44}	C_{66}	C_{12}	C_{13}	K	G	E	η
BCC_A2-1	283.5	283.5	153.2	153.2	244.7	244.7	221.3	70.2	190.5	0.357
BCC_A2-2	357.2	357.2	34.4	34.4	161.5	161.5	219.4	50.3	140.3	0.393
FCC_A1-1	292.2	292.2	143.2	143.2	186.3	186.3	219.1	96.1	251.6	0.309
HCP_A3-2	296.3	273.9	63.9	82.6	178.6	190.0	219.3	60.4	166.1	0.374
ALN	377.4	356.1	113.5	125.6	128.8	98.9	195.7	122.5	304.0	0.241
M23C6	447.4	447.4	115.6	115.6	220.3	220.3	296.0	114.8	304.9	0.328
LAVES_1	439.7	441.4	91.5	124.7	189.9	173.2	265.8	112.2	295.1	0.315
LAVES_2	441.7	429.6	50.4	106.4	233.3	200.4	285.1	80.7	221.2	0.371
Z_PHASE-1	318.2	281.5	68.4	72.3	150.1	175.0	212.5	68.1	184.6	0.355
Z_PHASE-2	318.0	419.8	79.9	16.6	142.9	168.6	212.5	60.3	165.2	0.370
SIGMA	400.9	400.9	57.3	57.3	197.7	197.7	265.0	72.2	198.6	0.375

FN5

Phase	C_{11}	C_{33}	C_{44}	C_{66}	C_{12}	C_{13}	K	G	E	η
BCC_A2-1	347.1	347.1	128.9	128.9	219.5	219.5	261.2	97.2	259.5	0.335
BCC_A2-2	353.3	353.3	38.2	38.2	184.2	184.2	238.1	52.0	145.4	0.398
FCC_A1-1	312.7	312.7	142.5	142.5	181.8	181.8	224.4	104.3	270.9	0.299
M23C6-1	440.0	440.0	124.6	124.6	223.1	223.1	295.4	117.9	312.2	0.324
M23C6-2	432.3	432.3	134.1	134.1	217.5	217.5	289.1	122.7	322.4	0.314
LAVES	441.5	395.6	79.6	106.8	228.2	205.7	283.4	94.8	255.8	0.350
NBNI3	290.2	305.9	113.3	111.4	178.2	152.7	205.6	90.9	237.7	0.307

HCM12

Phase	C_{11}	C_{33}	C_{44}	C_{66}	C_{12}	C_{13}	K	G	E	η
BCC_A2-1	190.3	190.3	139.5	139.5	292.4	292.4	122.3	362.1	546.7	-0.245
BCC_A2-2	354.9	354.9	32.9	32.9	163.2	163.2	212.9	46.0	128.8	0.399
FCC_A1-2	260.6	260.6	81.7	81.7	140.6	140.6	180.4	71.9	190.4	0.324
M23C6	445.4	445.4	134.0	134.0	217.9	217.9	293.7	125.5	329.5	0.313
LAVES	446.2	442.7	102.6	127.8	189.8	170.5	266.2	119.2	311.2	0.305
Z_PHASE	329.4	326.2	64.9	56.5	169.1	177.3	225.7	67.5	184.1	0.364
NBNI3	290.2	305.9	113.3	111.4	178.2	152.7	205.6	90.9	237.7	0.307

NF12

Phase	C_{11}	C_{33}	C_{44}	C_{66}	C_{12}	C_{13}	K	G	E	η
BCC_A2-1	280.0	280.0	134.7	134.7	236.1	236.1	226.3	66.8	182.4	0.366
BCC_A2-3	355.5	355.5	35.0	35.0	161.3	161.3	218.7	50.3	140.2	0.393
M23C6	441.3	441.3	115.7	115.7	223.5	223.5	296.1	112.9	300.5	0.331
LAVES	440.1	400.3	79.3	103.2	234.4	208.4	286.2	93.4	252.7	0.353
Z_PHASE-1	329.5	320.5	77.8	82.7	161.8	179.3	224.4	77.6	208.7	0.345
Z_PHASE-2	300.5	418.3	76.8	16.7	160.1	168.5	212.4	56.8	156.3	0.377
NBNI3	290.2	305.9	113.3	111.4	178.2	152.7	205.6	90.9	237.7	0.307

P122

Phase	C_{11}	C_{33}	C_{44}	C_{66}	C_{12}	C_{13}	K	G	E	η
BCC_A2-2	349.8	349.8	38.1	38.1	168.7	168.7	224.7	52.2	145.2	0.392
FCC_A1-1	288.9	288.9	144.4	144.4	195.8	195.8	222.7	91.8	242.2	0.319
ALN	377.4	356.1	113.5	125.6	128.8	98.9	195.7	122.5	304.0	0.241
M23C6	447.6	447.6	115.7	115.7	220.5	220.5	296.2	114.8	305.0	0.328
LAVES	445.1	426.9	65.8	104.6	235.6	203.0	288.1	88.8	241.6	0.360
Z_PHASE-1	318.4	333.3	82.1	78.1	178.9	166.0	221.2	78.6	210.9	0.341
Z_PHASE-2	301.5	418.0	81.0	24.2	145.2	170.7	215.1	64.4	175.7	0.364
NBNI3	290.2	305.9	113.3	111.4	178.2	152.7	205.6	90.9	237.7	0.307

P91

Phase	C_{11}	C_{33}	C_{44}	C_{66}	C_{12}	C_{13}	K	G	E	η
BCC_A2-1	284.9	284.9	124.8	124.8	232.0	232.0	231.5	66.4	181.7	0.369
BCC_A2-2	360.2	360.2	34.8	34.8	162.7	162.7	216.5	48.7	135.9	0.395
ALN	377.4	356.1	113.5	125.6	128.8	98.9	195.7	122.5	304.0	0.241
M23C6	447.5	447.5	115.6	115.6	220.5	220.5	296.1	114.7	304.9	0.328
LAVES	430.5	421.4	96.6	123.2	181.6	164.8	256.0	113.7	297.0	0.307
Z_PHASE	324.6	299.6	71.9	69.2	162.5	172.7	218.2	71.8	194.1	0.352
NBNI3	290.2	305.9	113.3	111.4	178.2	152.7	205.6	90.9	237.7	0.307

P92

Phase	C_{11}	C_{33}	C_{44}	C_{66}	C_{12}	C_{13}	K	G	E	η
ALN	377.4	356.1	113.5	125.6	128.8	98.9	195.7	122.5	304.0	0.241
NBNI3	290.2	305.9	113.3	111.4	178.2	152.7	205.6	90.9	237.7	0.307
M2B_TETR	439.8	504.1	141.7	135.6	199.5	190.1	282.1	137.0	353.6	0.291

T122

Phase	C_{11}	C_{33}	C_{44}	C_{66}	C_{12}	C_{13}	K	G	E	η
BCC_A2-1	269.7	269.7	145.4	145.4	249.8	249.8	190.3	56.9	155.2	0.364
BCC_A2-2	388.2	388.2	59.9	59.9	151.0	151.0	228.3	76.4	206.1	0.349
FCC_A1-2	296.8	296.8	145.5	145.5	189.5	189.5	222.7	97.6	255.5	0.309
ALN	377.4	356.1	113.5	125.6	128.8	98.9	195.7	122.5	304.0	0.241
M23C6	447.8	447.8	115.8	115.8	220.9	220.9	296.6	114.8	305.1	0.329
LAVES	444.7	393.4	79.5	106.9	231.1	206.1	284.5	94.8	255.9	0.350
Z_PHASE-1	332.6	301.9	77.8	71.1	169.8	176.4	222.4	74.2	200.3	0.350
Z_PHASE-2	318.6	417.0	76.9	8.8	145.4	167.2	193.7	50.6	139.6	0.380
NBNI3	290.2	305.9	113.3	111.4	178.2	152.7	205.6	90.9	237.7	0.307

X20

Phase	C_{11}	C_{33}	C_{44}	C_{66}	C_{12}	C_{13}	K	G	E	η
BCC_A2-1	191.6	191.6	139.5	139.5	293.5	293.5	122.9	364.6	550.0	-0.246
BCC_A2-3	372.8	372.8	48.2	48.2	178.7	178.7	242.4	63.8	175.9	0.379
FCC_A1-1	295.5	295.5	145.1	145.1	193.9	193.9	224.6	95.3	250.5	0.314
M23C6	438.4	438.4	132.6	132.6	219.7	219.7	292.6	122.7	323.0	0.316
LAVES	427.9	420.1	97.7	122.2	181.0	164.8	255.1	113.6	296.8	0.306
Z_PHASE	311.9	301.7	71.8	53.3	167.9	173.6	215.0	65.4	178.1	0.362

TB12

Phase	C_{11}	C_{33}	C_{44}	C_{66}	C_{12}	C_{13}	K	G	E	η
BCC_A2-2	305.3	305.3	44.5	44.5	189.8	189.8	227.6	49.1	137.4	0.399
HCP_A3-2	297.0	283.9	74.5	58.5	170.9	182.0	215.5	62.9	172.0	0.367
ALN	377.4	356.1	113.5	125.6	128.8	98.9	195.7	122.5	304.0	0.241
M23C6	442.8	442.8	113.8	113.8	222.4	222.4	295.8	112.3	299.1	0.332
LAVES	434.5	434.2	73.8	105.9	226.5	196.1	282.0	94.2	254.4	0.350
Z_PHASE-1	338.0	300.0	53.4	41.2	157.4	180.7	222.7	56.4	156.1	0.383
Z_PHASE-2	283.8	419.1	78.7	32.9	150.2	166.7	211.3	66.5	180.5	0.358
SIGMA	400.0	364.6	57.4	88.7	183.2	209.5	263.0	75.9	207.6	0.368
PI	281.9	270.7	82.3	77.6	171.6	163.9	203.4	69.6	187.5	0.346

VM12

Phase	C_{11}	C_{33}	C_{44}	C_{66}	C_{12}	C_{13}	K	G	E	η
BCC_A2-1	194.1	194.1	119.9	119.9	294.0	294.0	119.5	361.0	539.7	-0.253
BCC_A2-3	353.4	353.4	28.6	28.6	162.9	162.9	196.0	39.5	111.0	0.406
FCC_A1-1	307.1	307.1	144.5	144.5	181.2	181.2	221.9	103.5	268.8	0.298
M23C6	442.4	442.4	126.2	126.2	224.7	224.7	297.2	119.0	314.9	0.323
LAVES	441.0	402.0	78.6	103.2	235.0	209.8	287.4	93.1	252.0	0.354
Z_PHASE-1	352.5	279.3	83.6	61.0	163.3	188.4	228.4	73.4	198.9	0.355
Z_PHASE-2	310.9	413.8	79.7	26.5	150.5	168.0	217.8	65.9	179.5	0.363
PI	286.5	277.8	47.5	37.5	173.6	183.5	213.7	44.6	125.1	0.402

We checked elastic stability of all the phases presented in table 3 using method implemented in G(p,T). Only 3 phases which marked red on the table resulted in unstable. It is should be noted here that the calculated data are for the ground state and those unstable one could be stable in higher temperature and pressure and also in confinement. Further the phases which are stable based on elastic stability could be unstable in higher temperature and pressure conditions.

Among the BCC_A precipitate phases, BCC_A-1 has significantly smaller linear elastic constants (C_{11}) than that with BCC_A-2 and BCC_A-3 except in AXM steel. In AXM steel, C_{11} is about the same in both BCC_A-1 and BCC_A-2 precipitate phases. Interestingly, shear elastic constants C_{44} is significantly larger in BCC_A-1 phases than in the BCC_A-1 and BCC_A-2 except in AXM steel which has much larger C_{44} in BCC_A-2 than in BCC_A-1. In general, BCC_A-1 enhances shear elastic stiffness whereas BCC_A-2 and BCC_A-3 enhance linear elastic stiffness in the steel. AXM steel has two FCC_A1 phases, FCC_A1-1 and FCC_A1-3, elastic constants of FCC_A1-1 are significantly larger than that of FCC_A1-3. Other steel phases have only one FCC_A1 precipitate phase and have about the similar C_{ij} except HCM12 steel. Further detailed discuss about AXM steel are presented in later sections.

LAVES and $M_{23}C_6$ precipitation phases have large elastic constants in all steel phases. LAVES phases have hexagonal lattice but have small linear elastic anisotropy and significantly

larger shear elastic anisotropy. Z_PHASE precipitate phases which are in tetragonal lattice also have similar elastic constants in all steel phases. They have significantly smaller elastic constants than that of LAVES but have small linear and shear elastic anisotropy. More detailed results about LAVES phase are presented in the later sections.

Elastic anisotropy of ferritic steels phases is illustrated in Figure 4. Left figure show actual C_{11} and C_{33} values and also the linear elastic anisotropy in the structure. Line drawn represent for $C_{11} = C_{33}$. The data below the line means C_{11} is larger than C_{33} while data above the line means C_{33} is larger than C_{11}. Shear elastic constants C_{44} vs C_{66} are shown in right figure. Z-phase shows significantly higher C_{44} while the contrary is hold for LAVES phase.

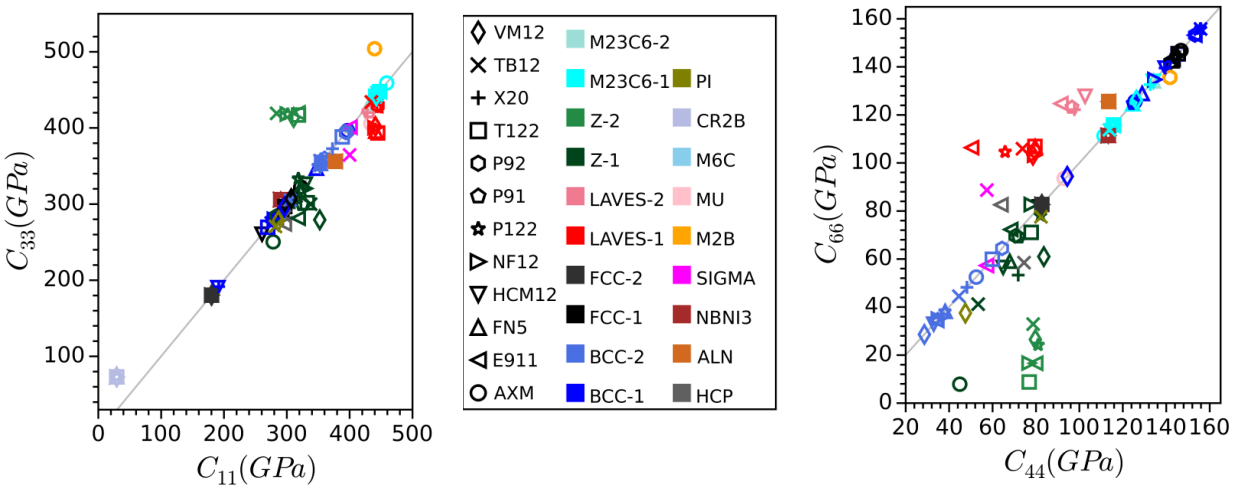

Figure 4. Elastic anisotropy of steel precipitate phases illustrated using C_{11}-C_{33} and C_{44}-C_{66}. (top) C_{11} vs C_{33} (bottom) C_{44} vs C_{66}. Symbols are for steel type and color for precipitate phase structure prototype. Line represent for $C_{11} = C_{33}$ (top) and C_{44}=C_{66} (bottom).

Bulk Mechanical Properties

Bulk modulus K and shear modulus data are shown in figure 5 (top). Over all bulk modulus K is significantly larger than shear modulus G in all precipitate phases except in Cr2B and BCC prototypes in HCM12 steel.

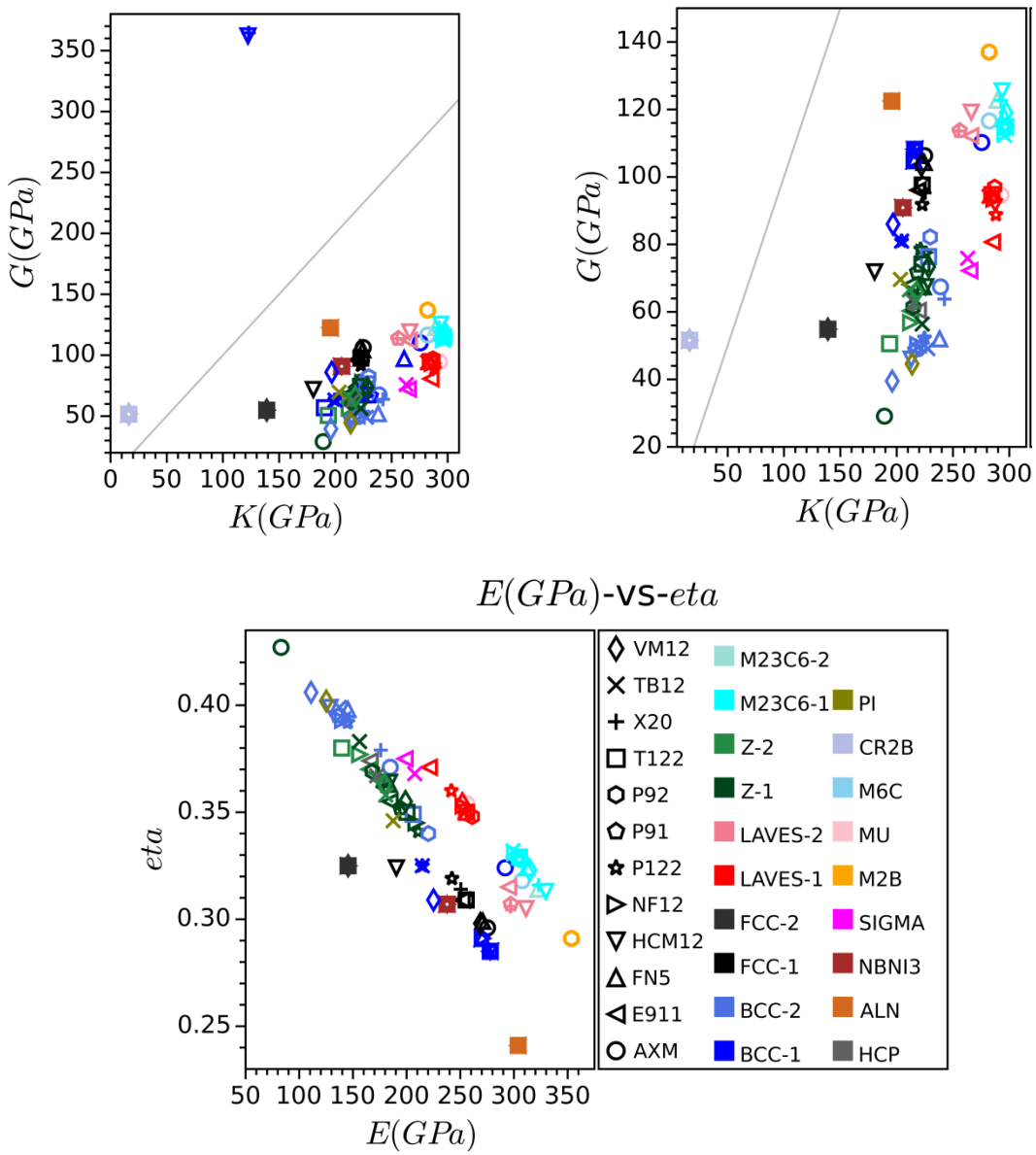

Figure 5. Calculated mechanical bulk properties. (top) Bulk modulus (K) vs shear modulus (G). Line represent for K = G.

Electronic Structure

As mentioned above, the precipitate phases AlN, NbNi3, and Cr2B are simple intermetallic phases. Figure 6 plots the density of states of these intermetallic phases. AlN phase is an insulator with a calculated band gap of 3 eV whereas NbNi3 and Cr2B are metals. The vertical line in figure 6 represents the top of valence band in insulator and semiconductors whereas Fermi level for metals. The density of states (states/Ev/cell) at Fermi level of NbNi3 is 1.62 which is much lower than 23.59 of Cr2B.

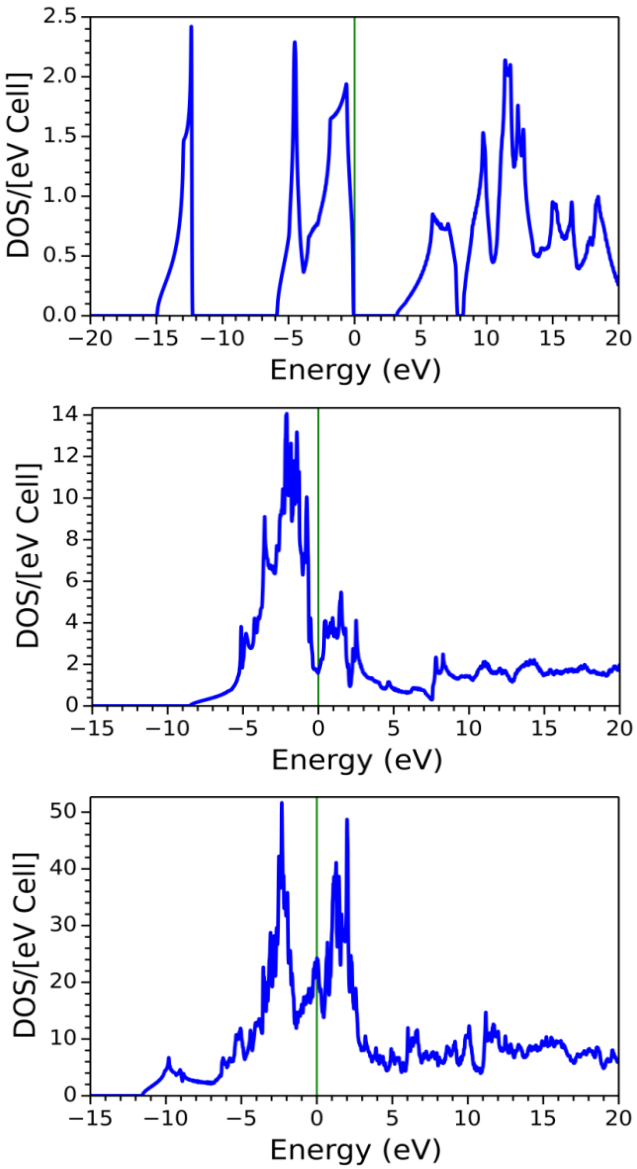

Figure 6. Density of states (DOS). (top) AlN, (middle) NbNi3, and (bottom) Cr2B.

AXM

Results for AXM steels had been calculated for all phases presented in the material. Tabel 4 listed structures of phases calculated.

Calculating elastic constants of solid solution was a challenge task. Special Quasirandom Structure (SQS) in the form of super cell is a cheap way to properties of solid solution without resorting to the computationally demanding cluster expansion method. SQS has local structures within a cutoff range resemble a completely random solid solution at high temperature. For present studies, we used the ***mcsqs*** program within the ATAT package to generate the SQS structure. Cutoff distance was default at 3.5Å. Local structures match up to 4-clusters.

Table 5. Phases presented in the AXM steel (only those elements with concentration >0.1% listed in the composition column)

Phase	Vol fract	Composition	Crystal	Microstructure
BCC-A2#2	0.8464	$Fe_{0.996}Si_{0.002}Al_{0.001}$	cI2	Matrix phase
BCC-A2#1	0.1006	$Cr_{0.957}Mn_{0.043}$	cI2	Precipitation
$M_{23}C_6$	0.0203	$(Cr_{0.864}Mn_{0.130}Fe_{0.006})_{23}C_6$	cF116	Precipitation
μ-Phase	0.0112	$(Fe_{0.992}Cr_{0.008})_7(W_{0.650}Mo_{0.350})_6$	hR39	Precipitation
FCC-A1#1	0.0100	$Ni_{0.584}Fe_{0.370}Si_{0.046}$	cF4	Precipitation
M_6C	0.0037	$(Mo_{0.992}W_{0.008})\,MoFe_2C$	cF112	Precipitation
Z-Phase	0.0051	$(Cr_{0.898}Fe_{0.102})VN_{0.669}$	tP6	Precipitation
$NbNi_3$	0.0010	Ni_3Nb	oP8	Precipitation
AlN	0.0012	AlN	hP4	Precipitation
FCC-A1#3	0.0003	$Cu_{0.999}Ni_{0.001}$	cF4	Precipitation
M_2B	0.0003	$(Mo_{0.953}Cr_{0.047})_2B$	tI12	Precipitation

For all solid solution phases, only elements with larger than 0.4% concentration were included in the calculation as we limited our calculations to models with less than 250 atoms. Exactly matching the experiments determined concentration was not possible with the size

limited. Instead we rounded the concentrations to the nearest integer to ensure every lattice site was fully occupied. We plan to compute models with concentrations near the experimental values (ups and downs) and use interpolation scheme to better estimate the elastic constants. For dilute dopants, we may use the scaling law to estimated the elastic constant ($E \propto c^{1/2}$).

All calculations were carried out using the G(p,T) package which employed VASP as the first-principles computing engine. For comparison, cutoff energies were all at 400eV. Several phases including BCC-A2#1 were calculated using spin-polarized setting.

Table 6. Elastic constants results of known phases in AXM steel (GPa).

Phases	C_{11},C_{22},C_{33}	C_{44},C_{55},C_{66}	C_{12},C_{13},C_{23}	K	G	E	ν	G/K
BCC-2#1	376 433	42 73	232 135	239	67	185	0.371	0.282
BCC-A2#2	330 estimated	110 estimated	171 estimated	224	97	253	0.311	0.433
AlN	482 780	-31 155	168 -58	169	555			
FCC-A1#1	322	147	179	225	106	275	0.296	0.473
$M_{23}C_6$	459	111	216	297	115	306	0.328	0.388
M_2B	440 504	141 136	199 190	282	137	353	0.291	0.486
M_6C	442	115	203	282	117	308	0.318	0.413
μphase	442 426 406	92 94 94	245 225 217	293	95	256	0.354	0.323
$NbNi_3$	290 305	113 111	178 153	206	91	238	0.307	0.442
Zphase	278 250	45 8	180 167	189	29	83	0.427	0.154

Macroscopic mechanical properties of Steel depend on multiple scale structures. At atomic scale, structures are largely determined by thermodynamics. First principles can be used to estimate their properties. At micro scale, structures are largely determined by processing whose

effects on properties can be difficult to evaluate. Homogenization provides means to estimate properties of multi-phase materials based on atomistic properties and microstructure.

K = 228 GPa, G = 94GPa, E = 249GPa and ν = 0.318

LAVES Phase

LAVES phases play an important role in ferritic steels. In general, they have high strength, low density and high melting point [1]. Themselves are also promising for superconducting, magnetic and hydrogen storage materials [2, 3, 4].

Precipitation of LAVES phases is common in steels. They affect physical properties of steels significantly. There are conflicting assessments of the effect of LAVES phases in steel creep resistance, some find detrimental [5, 6, 7]to creep strength and others find beneficial to creep strength [8, 9]. Both could be true as there are wide varieties of LAVES phases in different lattice symmetry and with 2 or more elements in them as different set of elements in LAVES phase could result in significantly different physical properties.

So far only binary LAVES phases are studied extensively [10, 11, 12] along with some cases of ternary LAVES phases [13]. In this study, we presented the LAVES solid solutions covering binary to 5 elements of the set of Mo, W, Fe, Cr, Si in hexagonal C14 symmetry (MgZn2). Two elements Mo and W takes the Mg site whereas Fe, Cr, and Si in Zn site.

Heat of Formation

We calculated the total energy of individual elements to check whether the solid solution phases are energetically favored. The difference in total energy of laves solid solution phase to the sum of total energies of individual elements (ΔE) are shown in the ternary plot Fig. 7. There are 40 phases with positive ΔE and 85 phases with negative ΔE. Among the phases with +ve ΔE,

5 phases have ΔE less than 0.9 eV. In general ΔE is positive for larger concentration of either of Fe, Cr, or Si. It is worth to note in the figure that data for Cr=1.00 for Mo=0.00 and Si=1.00 are not included as those phases have very large positive ΔE and they were also elastically unstable. Most of the high concentration Cr phases have large +ve ΔE and increasing Mo concentration appears to increase large +ve ΔE region in higher Cr concentration. The most energetically favorable phases are around Fe = 0.5, and Si=0.5. As the Mo concentration increases, the most energetically stable region (more –ve ΔE blue region) grows and shifts towards smaller concentration of Fe and larger concentration of Si. This indicates, Mo favors Si where as W favors Fe energetically.

Elastic and Mechanical Properties

The calculated elastic constants, mechanical bulk properties and ΔE are presented are plotted as the ternary phases for different concentration of Mo. The ternary figures from Fig. 8 to Fig. 11 show how the elastic constants change with Fe, Cr and Si concentration for a given Mo (W) concentration. Elastic constants of LAVES phases vary widely with different concentration of comprising elements. The range of minimum to maximum is quite large. Linear elastic constant C11 (Fig. 8) is larger for larger Fe concentration around Fe=1.00 and smaller for larger concentration of Si. When Mo concentration increases the region of larger C11 around Fe=1 shrinks and the region of smaller C11 at larger Si concentration swells. Decrease in C11 with increasing Mo concentration at larger Fe concentration is quite large. Change in C33 (Fig. 9) with different elemental concentration is similar to that of C11 but in contrast to C11, the region of larger C33 is quite larger at around Fe=0.7 and rapidly shrinks with increasing Mo concentration. For Mo=0.00, the region of smaller C33 at larger Si concentration is small. For

Mo concentration of 0.25, this region grows and appears independent of further increase in Mo concentration. Shear elastic constants C44 (Fig. 10) and C66 (Fig. 11) also show similar pattern as in C11 and C33. The region of larger C44 is around Fe=0.65 and decreases with increasing Mo concentration whereas the regions of smaller C44 are around larger Cr and Si concentration and do not show clear trend with increasing Mo. The region of larger C66 is much larger than that of C44 and extends from Fe = 0.45 up to Fe = 1.00 and decreases with increasing Mo concentration.

Fig. 12 shows how calculated bulk modulus (K) changes with Fe, Cr, and Si concentration for a give Mo (W) concentration. In contrast to elastic constants, K is larger for larger Cr concentration and decreases with increasing Mo concentration. The K is smaller for larger Si concentration and difference between the largest and the smallest K is quite large. The region of smaller K is quite small for Mo=0.00 and grows with increasing Mo concentration. On the other hand shear modulus (G) and Young's modulus (E) (Fig. 13 and Fig. 14) both are larger for larger Fe concentration and smaller for larger Cr and Si concentration. The region of larger G and E shrinks with increasing Mo concentration. Poison's ratio (η) (Fig. 15), which is calculated from the K and G using the equation as shown above in method section, represents resistant to change in bond length in relation to resistant to change in bond angle. Poisson's ratio is larger for larger Cr and Si concentration and smaller for larger Fe concentration. Smaller η region concentrated more towards higher Fe concentration extends to smaller Fe concentration for increased Mo. Fig. 16 shows the G/K data which could indicate the relative ductility or brittleness of the structure. Larger G/K means greater resistant to change in bond angle leading relatively more brittleness of the structure. On the other hand smaller G/K means easier to change in bond angle resulting in increased ductility in the structure. As can be seen the Fig. 16, G/K is larger for larger Fe

concentration and smaller for larger Cr concentration. So for a given concentration of Mo (W), the larger concentration of Fe results in relatively more brittle structure whereas larger concentration of Cr and Si results in increased ductility in the structure. Change in Mo/W concentration shows no significant effect in G/K, so is little effect in ductility of the LAVES structures.

Elastic anisotropy shows directional dependence of strain-stress response in material. While anisotropic material could potentially useful in some applications, but it could result in problem in composites because of directional effect of compression and expansion under stress. Elastic anisotropy of LAVES phases varies with the constituent elements and their concentration. The linear elastic anisotropy and shear elastic anisotropy factors of LAVES phases are showed in Fig 17 and Fig 18 respectively. We calculated linear and shear elastic anisotropy factors form elastic compliance tensor as suggested by Desmond Tromans [23]. Anisotropy of LAVES seems not dependent on the concentration of Mo or W, but depends on Cr, Fe, and Si concentrations. LAVES phase is more anisotropic for larger concentration of either of Fe, Cr, or Si whereas the phases with all three elements in close proportions results in more isotropy in both linear and shear elastic behavior.

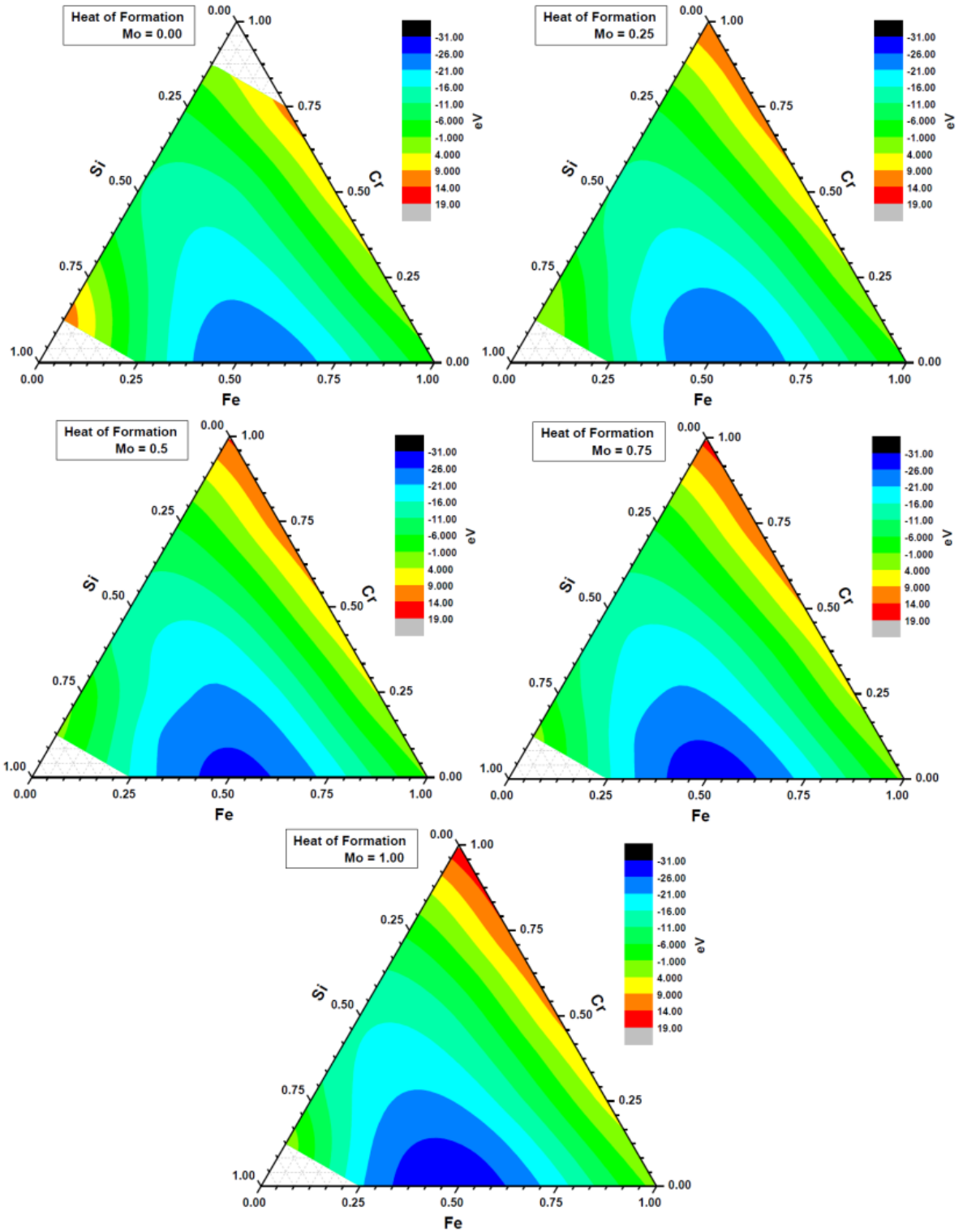

Figure 7. Heat of formation of the Ternary Laves phase Fe-Cr-Si.

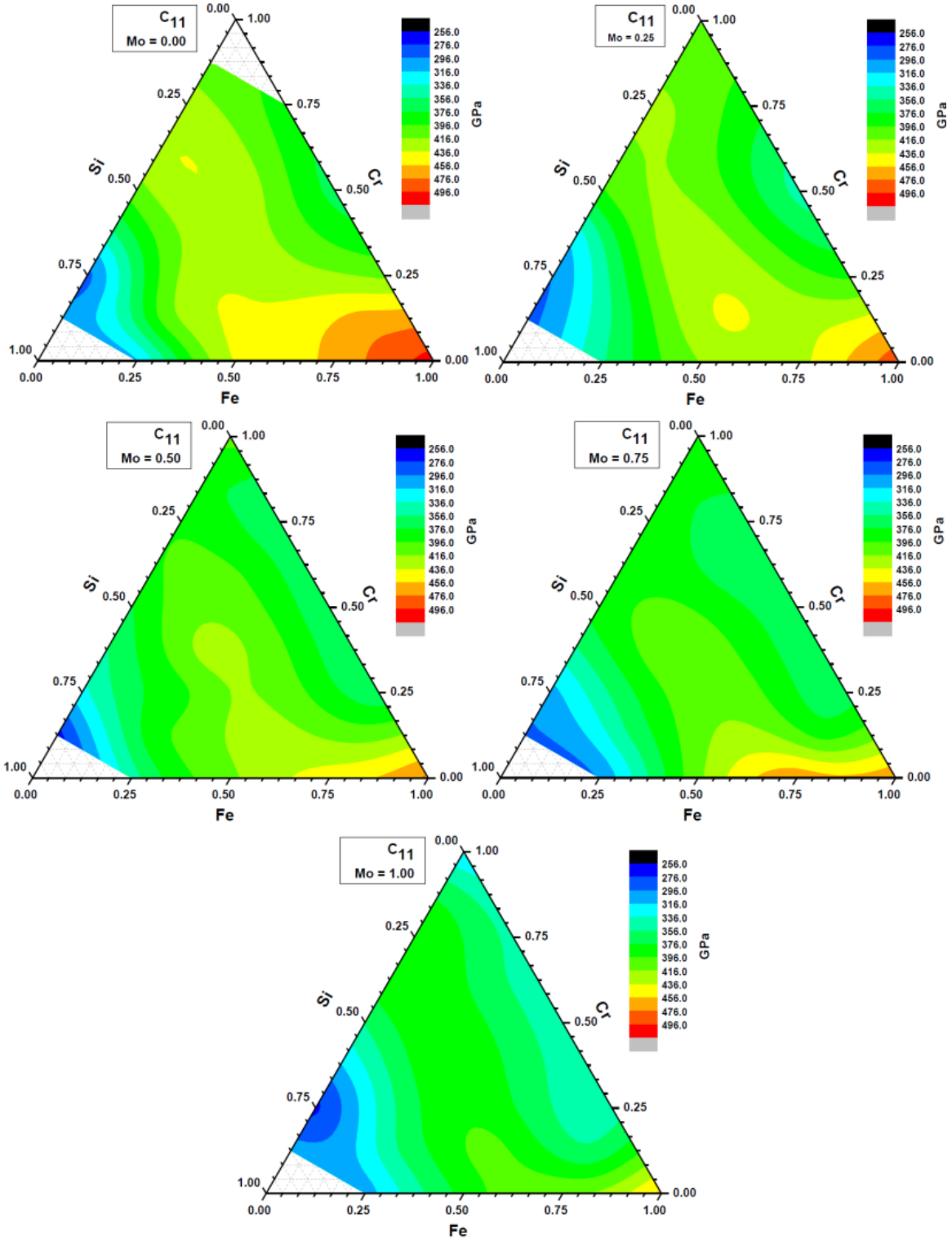

Figure 8. C_{11} of the Ternary Laves phase Fe-Cr-Si.

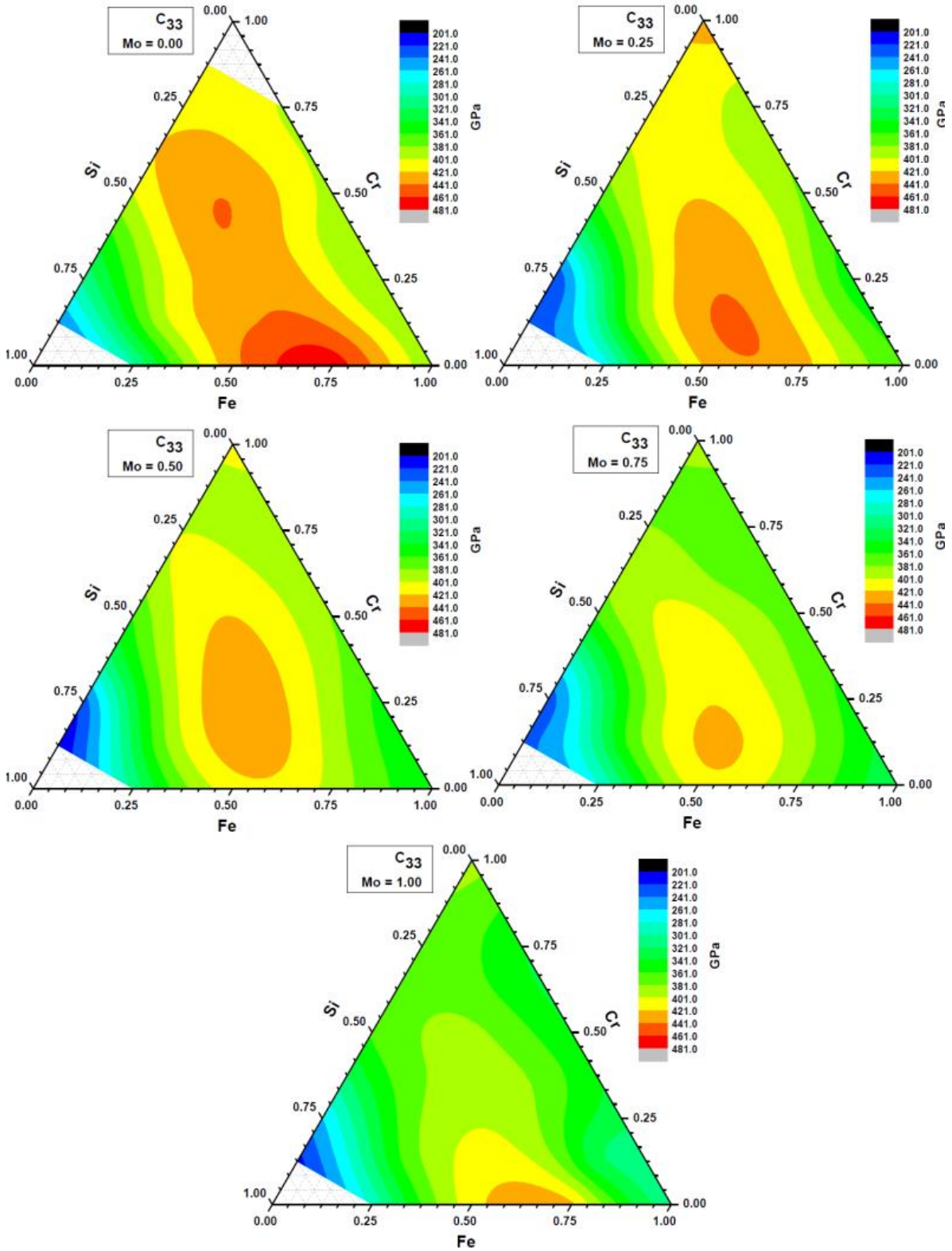

Figure 9. C_{33} of the Ternary Laves phase Fe-Cr-Si.

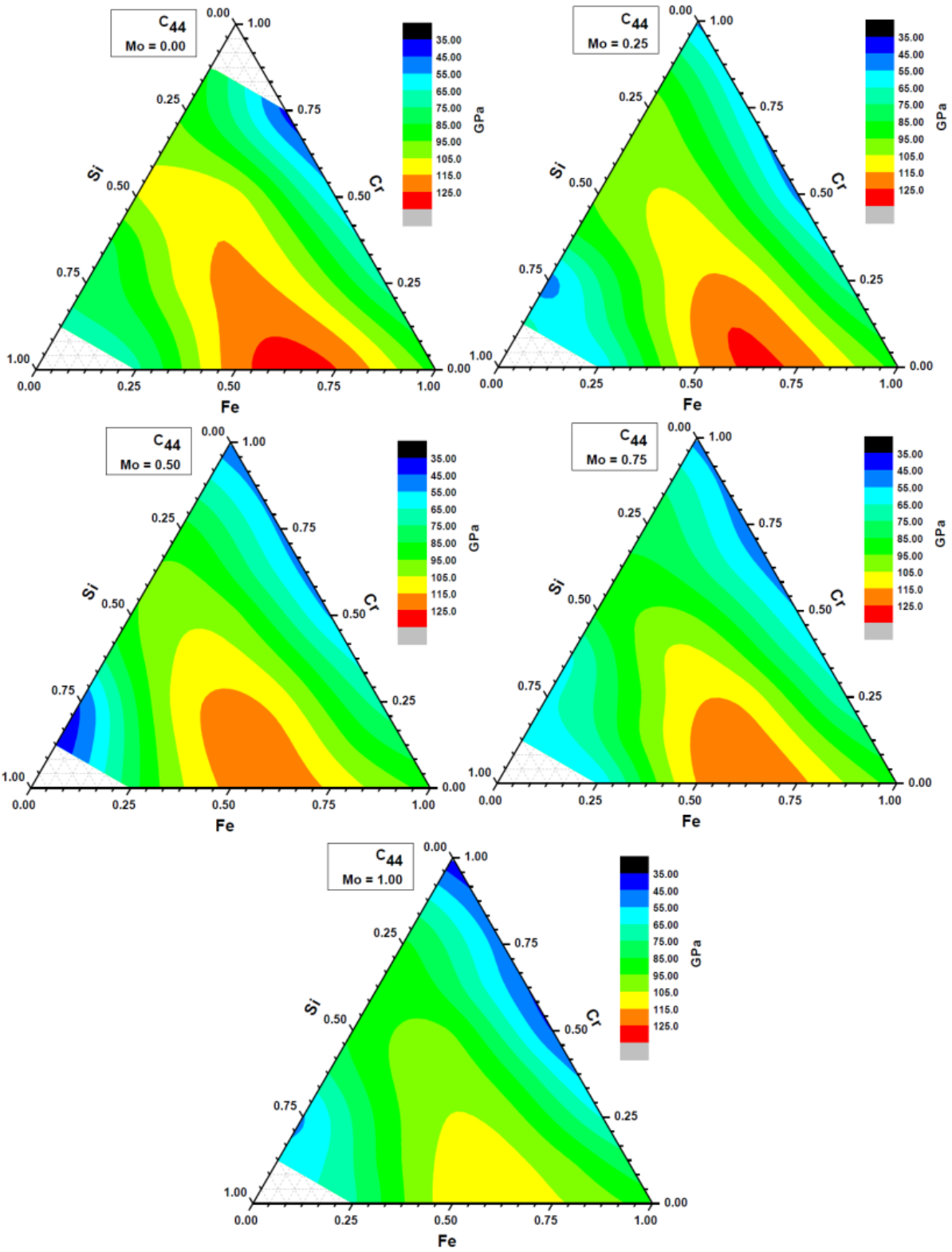

Figure 10. C_{44} of the Ternary Laves phase Fe-Cr-Si.

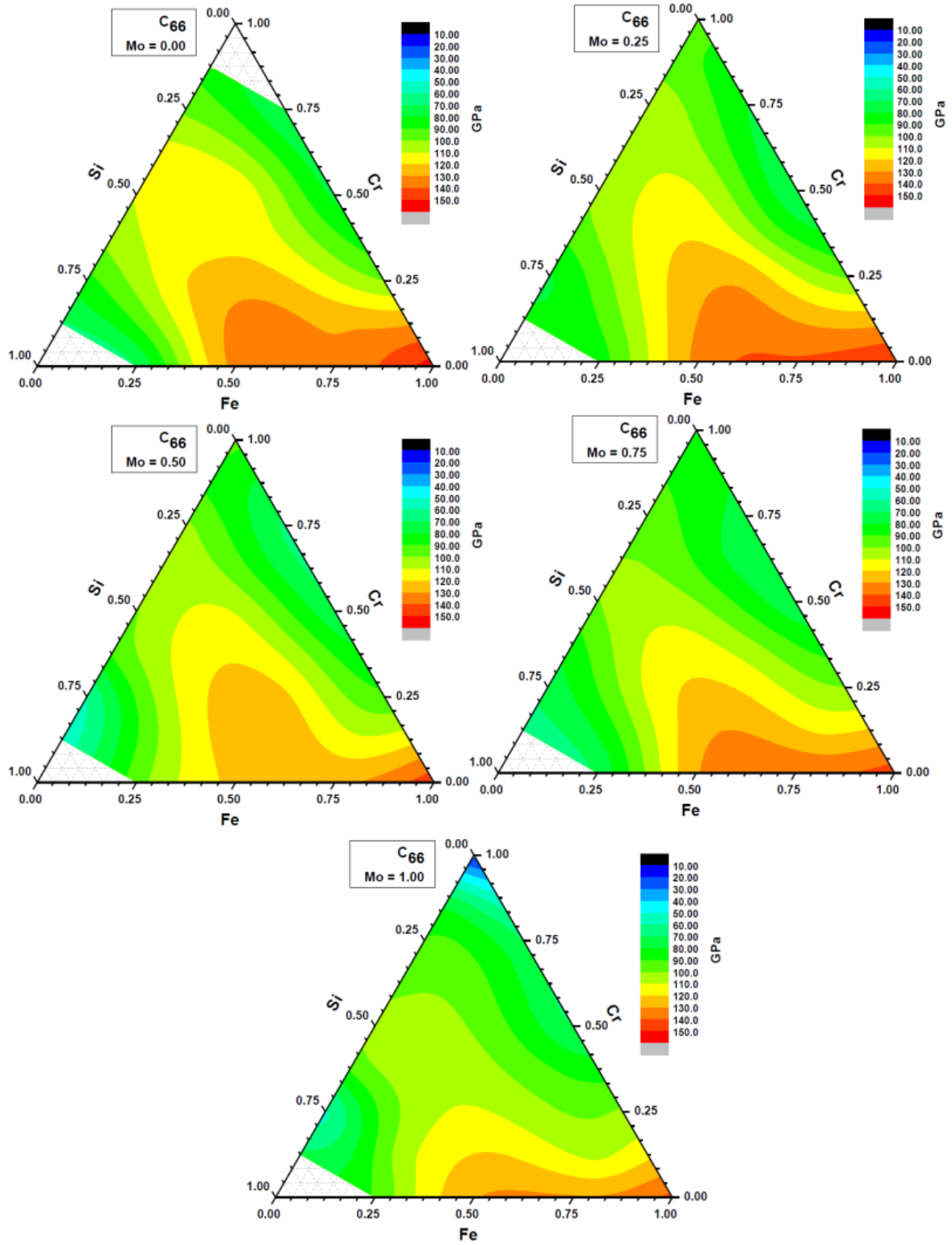

Figure 11. C_{66} of the Ternary Laves phase Fe-Cr-Si.

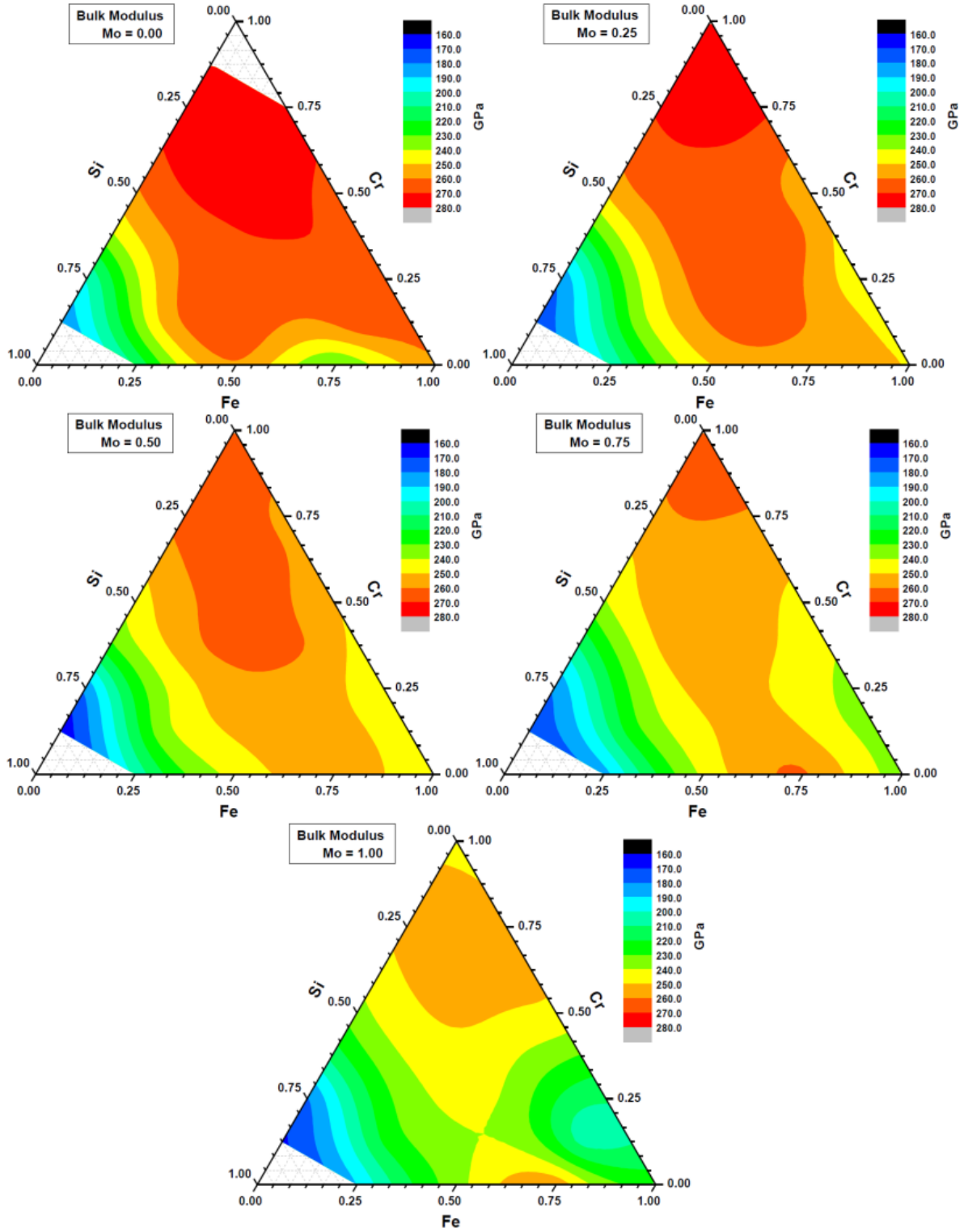

Figure 12. Bulk modulus of the Ternary Laves phase Fe-Cr-Si.

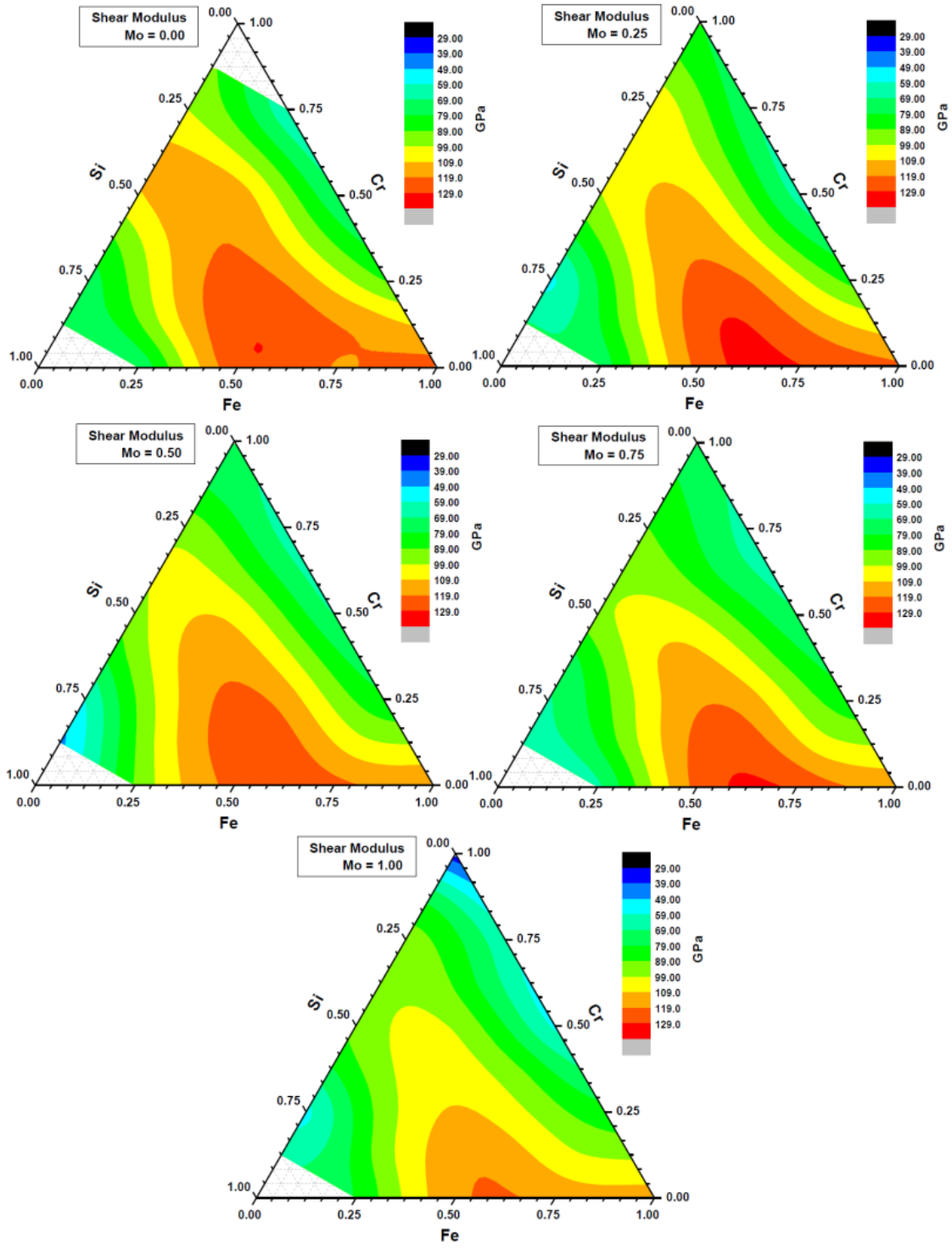

Figure 13. Shear modulus of the Ternary Laves phase Fe-Cr-Si.

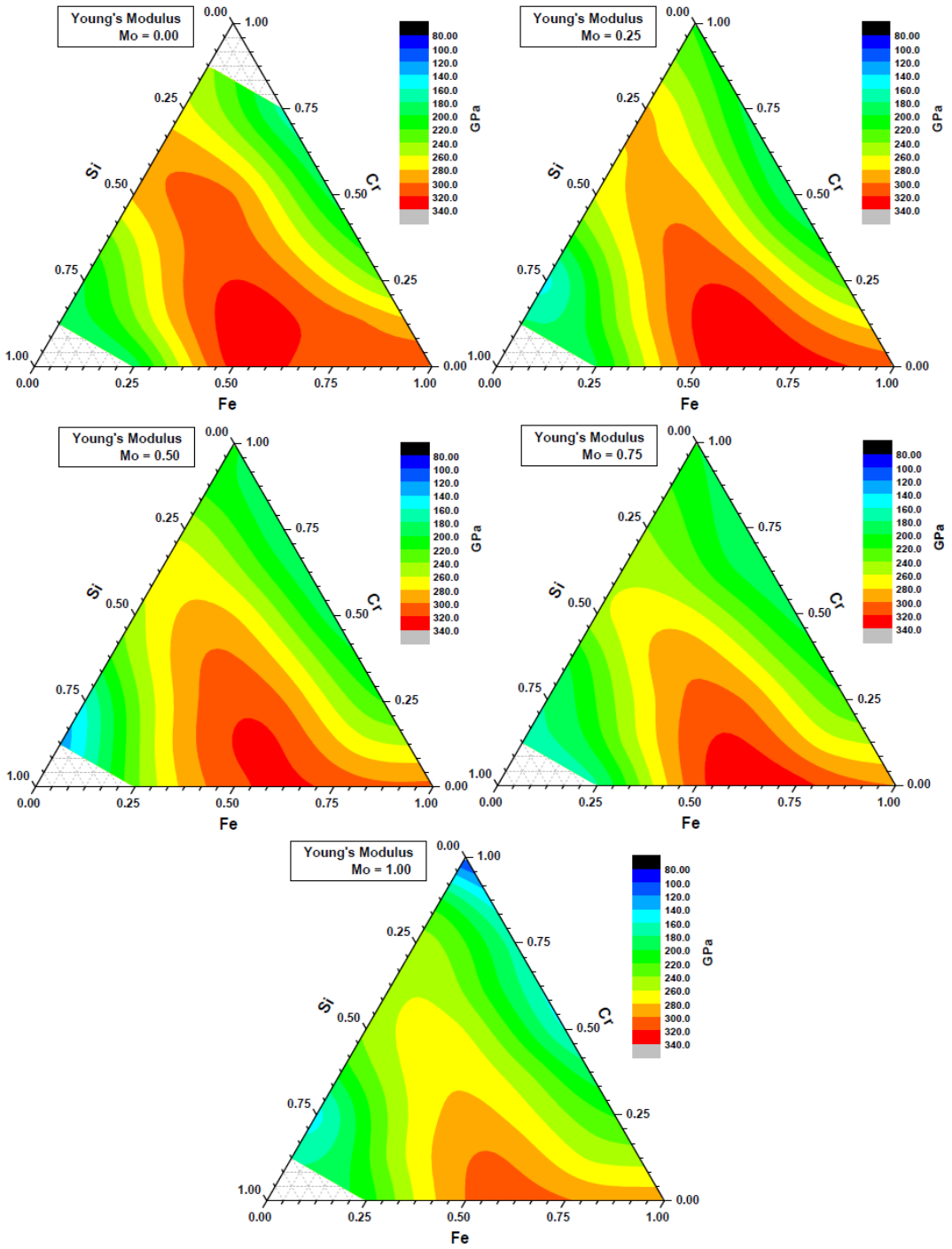

Figure 14. Young's modulus of the Ternary Laves phase Fe-Cr-Si.

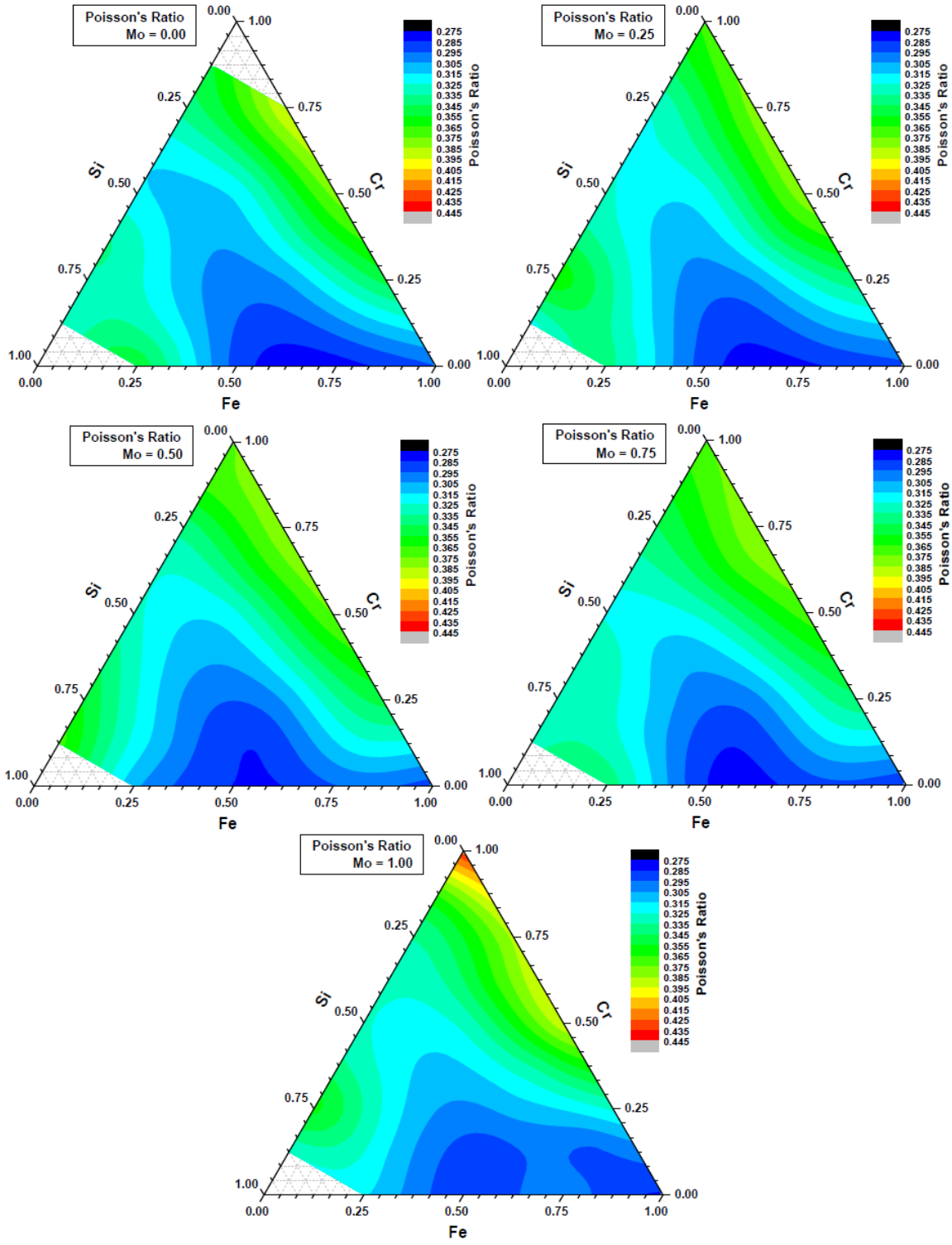

Figure 15. Poisson's ratio of the Ternary Laves phase Fe-Cr-Si.

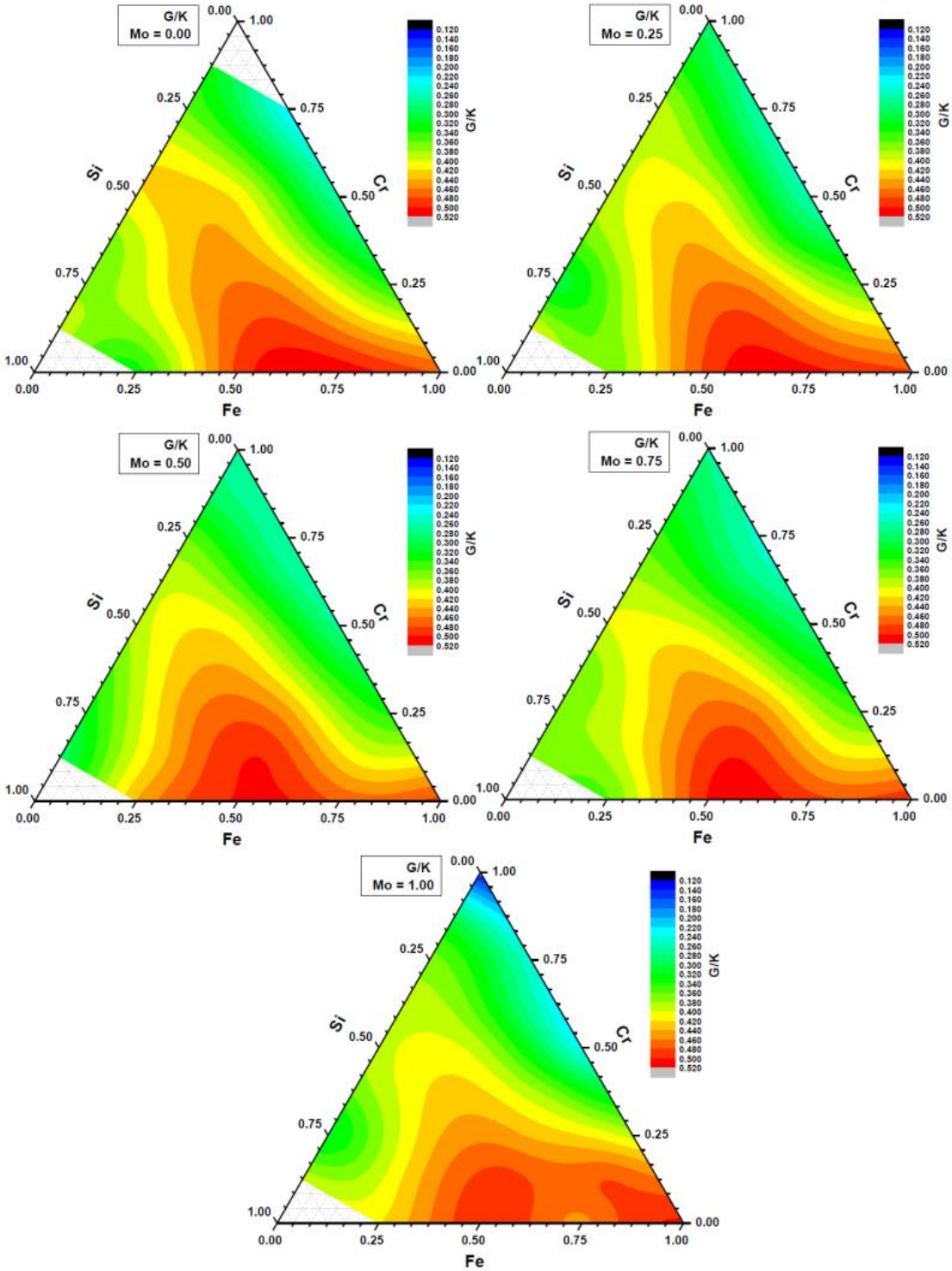

Figure 16. G/K ratio of the Ternary Laves phase Fe-Cr-Si.

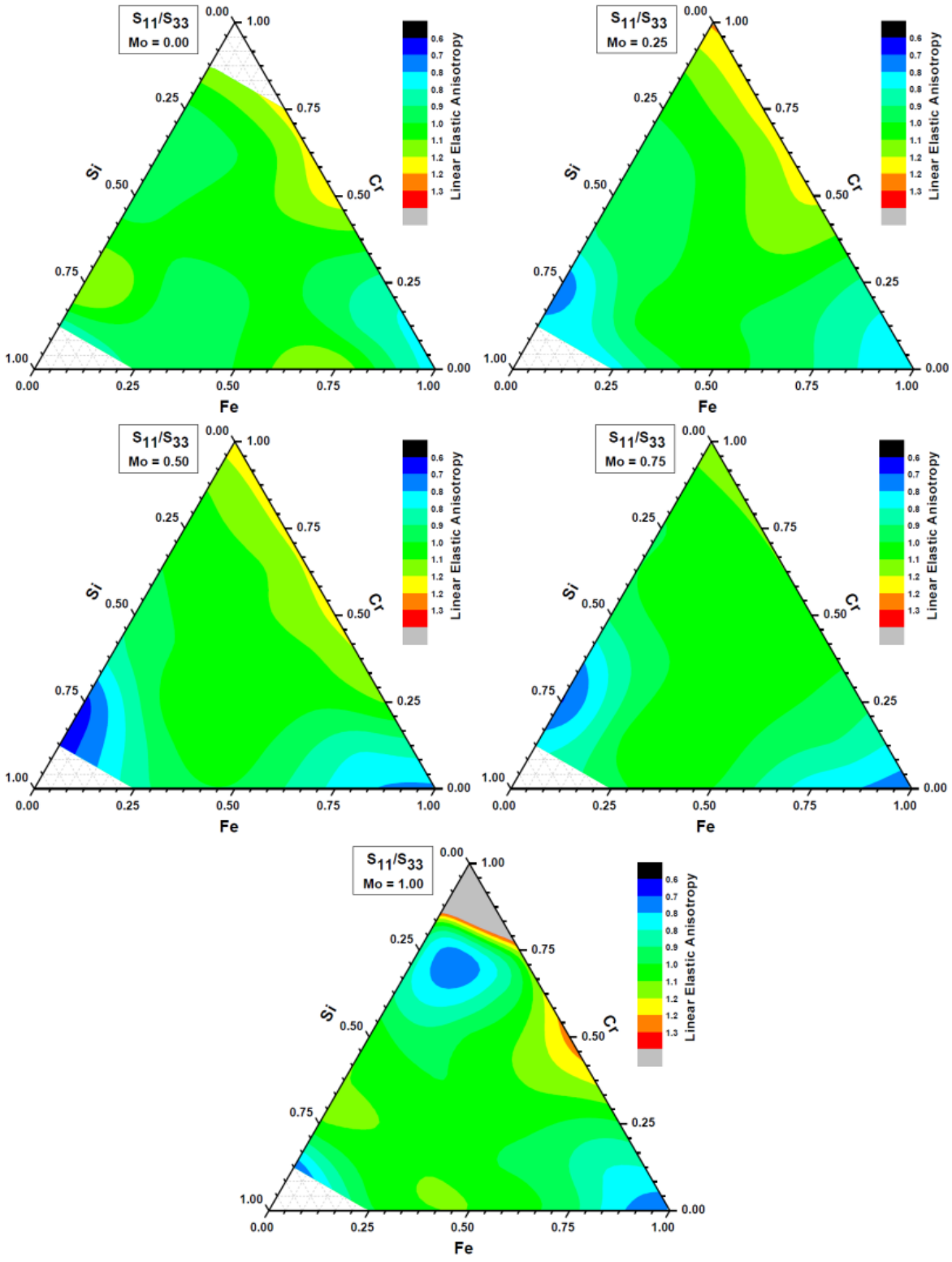

Figure 17. S_{11}/S_{33} of the Ternary Laves phase Fe-Cr-Si.

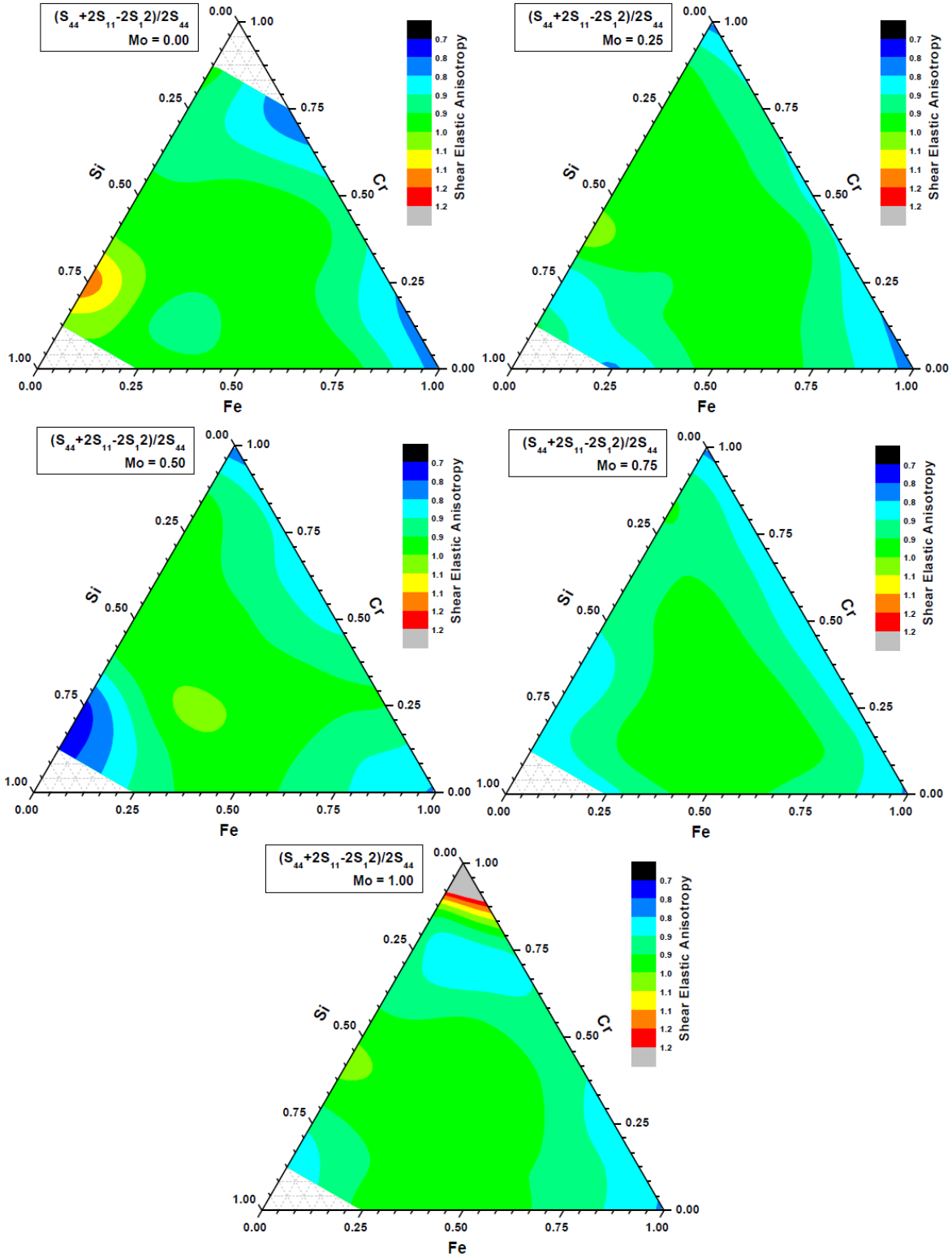

Figure 18. $(S_{11}+S_{44}-2S_{12})/2S_{44}$ of the Ternary Laves phase Fe-Cr-Si.

Summary

We calculated elastic and mechanical properties of LAVES phase solid solution comprising of 5 elements, Mo,W, Fe, Cr, Si, in hexagonal C14 symmetry. This is the first of this type of calculations that span form binaries to phases with 5 elements in it. Using elastic stability and heat of formation criteria, we identified the unstable and stable phases. Calculated elastic and mechanical properties are found to be significantly dependent on concentration of comprising elements. In general, elastic stiffness constants are larger for larger Fe concentration and decreases with increasing Mo concentration. Bulk modulus (K) is larger for larger Cr concentration whereas both shear modulus G and Young's modulus (E) are larger for larger Fe concentration. W enhances elastic and mechanical bulk properties whereas Mo degrades. Calculated η and G/K ratio indicate increased Cr concentration may result in relatively more ductility in the LAVES phase structure. Elastic anisotropy of the phase does not depend on Mo/W whereas the phase is closer to isotropy when Fe, Cr, and Si are comparable proportions.

References for this section only:

[1] J. Livingston, "Laves-phase superalloys?," Phys. Sat. Sol (a), vol. 131, no. 2, p. 415, 1992.
[2] B. M. Klein, W. E. Picket, D. A. Papaconstantopopoulos and L. L. Boyer, "Electronic structure, superconductivity, and magnetism in the C15 compounds ZrV2, ZrFe2, and ZrCo2," Physical Review B, vol. 27, p. 6721, 1983.
[3] X. Q. Chen, W. Wolf, R. Podloucky, P. Rogl and M. Marsman, "Ab initio study of ground-state properties of the Laves-phases compund ZrMn2," Physical Review B, vol. 72, p. 054440, 2005.
[4] A. V. Skripov, T. J. Udovic and J. J. Rush, "Hydrogen jump diffusion in C14-type ZrMn2H3: Quasielastic neutron scattering study," Physical Review B, vol. 76, p. 104305, 2007.
[5] Y. Hosoi, N. Wade, S. Kunimitsu and T. Urita, J. Nucl. Mater., vol. 461, p. 141, 1986.
[6] K. Miyahara, J.-H. Hwang and Y. Shimoide, Scr. Metall. Mater., vol. 32, p. 1917, 1995.
[7] S. Kunimitsu, T. Iwamoto, A. Hotta, Y. Sasaki and Y. Hosoi, in Proc Int. Conf. on Stainless Steels, , Chiba , 1991.
[8] J. Hald, Steel Res., vol. 9, p. 369, 1996.

[9] I. Fedorova, A. Belyakov, P. Kozlov, V. Skorobogatykh, I. Shenkova and R. Kaibyshev, "Laves-phase precipitates in a low-carbon 9% Cr martensitic steel during aging and creep at 923 K," Materials Science and Engineering A, vol. 615, p. 153, 2014.
[10] X.-Q. Chen, W. Wolf, R. Podloucky, P. Rogl and M. Marsman, "Ab initio study of ground-state properties of the Laves-phases compound ZrMn2," Phys. Rev. B, vol. 72, p. 054440, 2005.
[11] F. Sun, J. Zhang, S. Mao and X. Han, "Structural, electronic and elastic properties of the C14 NbCr2 Laves phases under hydrostatic pressure," Silid State Communications, vol. 174, p. 46, 2013.
[12] Y.-P. Xie, Z.-Y. Wang and Z. F. Hou, "The phase stability and elalstic proiperties of MgZn2 and Mg4Zn7 in Mg-Zn alloys," Scripta materialia, vol. 68, p. 495, 2013.
[13] X. Yan, A. Grytsiv, P. Rogl, H. Schmidt and G. Giester, "Teh ternary Laves phase Nb(Ni1-xAlx)2 with MgZn2-type," Computer Coupling of Phase Diagrams and Thermochemestry, vol. 33, p. 11, 2009.
[14] A. v. d. Walle, P. Tiwary, M. d. Jong, D. L. Olmsted, M. Asta, A. Dick, D. Shin, Y. Wang, L.-Q. Chen and Z.-K. Liu, "Efficient stochastic generation of special quasirandom structures," Calphad Journal, vol. 42, p. 13, 2013.
[15] G. Kresse and J. Furthmuller, "Efficiency of ab-initio Total Energy Calculations for Metals and Semiconductors Using a Plane-wave Basis Set," Comput. Mater. Sci., vol. 6, p. 15, 1996.
[16] G. Kresse and J. Hafner, "Ab initio Molecular Dynamics for Liquid Metals," Phys. Rev. B, vol. 47, p. 558, 1993.
[17] G. Kresse and J. Furthmuller, "Efficient iterative Schemes for ab initio Total-Energy Calculation Using Plane-Wave Basis set," Phys. Rev. B, vol. 54, p. 11169, 1996.
[18] P. E. Blöchl, "Projector Augmented-Wave Method," Phys. Rev. B, vol. 50, p. 17953, 1994.
[19] G. Kresse and J. Joubert, "From Ultrasoft Pseudopotentials to the Projector Augmented Wave Method," Phys. Rev. B , vol. 59, p. 1758, 1999.
[20] W. Voight, Lehrbuch der Kristallphysik. Taubner, Leipzig, 1928.
[21] A. Reuss and Z. Angew, "Berchung der Fiessgrenze von Mischkristallen auf Grund der Plastizia tsbedingung fur Einkristalle," vol. 9, p. 55, 1929.
[22] R. Hill, "The Elastic Behaviour of a Crystalline Aggregate," Proc. Phys. Soc. Lond., vol. 65, p. 350, 1952.
[23] Desmond Tromans, "Elastic Anisotropy OF HCP Metal Crystals and Polycrystals ", IJRRAS 6 (4), 462 (2011)

B.2 Screening studies for Better Ferritic Steel Design

The overall elastic properties of know 9-12Cr ferritic steels were computed using our *homogenize* script. Note that precipitation microstructure details were ignored in current implementation. Elastic properties are assumed to be independent of particle sizes and shape.

Table 7. Computed elastic properties of ferritic steel composite (unit: GPa)

Steel	K	E	G	ν
AXM	271.1	272.1	102.1	0.3327
P92	251.4	228.0	84.5	0.3488
T122	253.0	238.2	77.0	0.3592

Direct search for better ferritic steels require additional information, for example, phase composition for a given element chemical composition. Chang in chemical composition could also lead to precipitation of new phases and elimination of phases. For solid solution phase, its chemical composition can also be altered. Moreover, microstructure can also change. However, assuming no significant change to microstructure, the method developed in present study provided a method to assess the effect on overall mechanical properties of such a complex multi-component multi-phase metal from properties of phases found in the system.

CONCLUSIONS

In conclusion, we developed software packages to enable large scale screening of complex multi-component multi-phase materials under certain constraints. Given phase composition and structure, volume fraction, our package can efficiently carry out large number of calculations at first principles quality. We implemented software modules in our G(p,T) package: (1) module that automates the solid solution modeling based on structure template and composition parameters; (2) module that automate the physical properties calculations using special quasirandom structure methods; (3) Homogenize script based on Eshelby inclusion theory.

We calcuated all known phases found in ferritic steels of which majorities are solid solution phases. Many solid solution phases were for the first time systematically studied using first principles methods. We assessed the zero temperature elastic properties of known 9-12Cr ferritic steels using Eshelby's inclusion theory for multiphase multicomponent system. The shear/bulk modulus ratio are used to indicate the ductility of the ferritic steel;

.

V.FACILITIES AND RESOURCES

We have upgraded our cluster to dual Xeon 8-core (24 nodes) and 16-core systems (7 nodes). Among them, 30 nodes are dedicated to computing, 1 node serves as head node that provides internet interface and cluster management, and 1 original node is kept for storage service. Each computing node has 32-128GB memory. All computer nodes use a small 40-60GB solid state disk for boot and temporary scratches. An 8TB and an 28TB storage array are used to provide the shared home and scratch cluster file system.

REFERENCES,

[1] B. Bewlay, M. Jackson, P. Subramanian, J. Zhao, Metallurgical and Materials Transactions A 34 (2003) 2043-2052.
[2] C. Bouillet, D. Ciosmak, M. Lallemant, C. Laruelle, J.J. Heizmann, Solid State Ionics 101-103 (1997) 819-824.
[3] M.J. Davidson, M. Biberger, A.K. Mukherjee, Scripta Metallurgica et Materialia 27 (1992) 1829-1834.
[4] K. Zelenitsas, P. Tsakiropoulos, Materials Science and Engineering: A 416 (2006) 269-280.
[5] J. Geng, P. Tsakiropoulos, Intermetallics 15 (2007) 382-395.
[6] J. Geng, P. Tsakiropoulos, G. Shao, Materials Science and Engineering: A 441 (2006) 26-38.
[7] Y.X. Tian, J.T. Guo, Y.C. Liang, C.L. Wu, L.Z. Zhou, H.Q. Ye, International Journal of Materials Research 98 (2007) 511-515.
[8] J.T. Guo, Y.X. Tian, G.M. Cheng, L.Z. Zhou, L.L. He, H.Q. Ye, Journal of Alloys and Compounds 470 (2009) 606-609.
[9] W.-Y. Kim, H. Tanaka, A. Kasama, R. Tanaka, S. Hanada, Intermetallics 9 (2001) 521-527.
[10] S. Miura, K. Ohkubo, T. Mohri, Intermetallics 15 (2007) 783-790.
[11] H. Lukas, S.G. Fries, B. Sundman, Computational Thermodynamics: The Calphad Method, Cambridge University Press, New York, 2007.
[12] G. Kresse, J. Furthmuler, Computational Materials Science 6 (1996) 15-50.
[13] G. Kresse, J. Furthmuler, Physical Review B 54 (1996) 11169.
[14] G. Kresse, J. Hafner, Physical Review B 47 (1993) 558.
[15] H. Yao, L. Ouyang, W.-Y. Ching, Journal of the American Ceramic Society 90 (2007) 3194-3204.
[16] L. Ouyang, W.-Y. Ching, physica status solidi (b) 242 (2005) R64-R66.
[17] L. Ouyang, W.Y. Ching, Journal of Applied Physics 95 (2004) 7918-7924.
[18] L. Ouyang, S. Aryal, P. Rulis, W.Y. Ching, (2008).
[19] M. Friák, M. Šob, V. Vitek, Physical Review B 68 (2003) 184101.
[20] T. Li, J.W. Morris, D.C. Chrzan, Physical Review B 70 (2004) 054107.
[21] M. Černý, J. Pokluda, Physical Review B 82 (2010) 174106.
[22] D.W. Feldman, J.H. Parker, W.J. Choyke, L. Patrick, Phys. Rev. 173 (1968) 787-&.
[23] M.W. Chase, NIST-JANAF Thermochemical Tables, 1998.
[24] P.s.f.D.C.C. http://www.dow.com.
[25] Z. Li, R.C. Bradt, J. Mat. Sci. 21 (1986) 4366-4368.
[26] Z. Li, R.C. Bradt, J. Am. Cera. Soc. 70 (1987) 445-448.
[27] M. Stockmeier, R. Müller, S.A. Sakwe, P.J. Wellmann, A. Magerl, J. Appl. Phys. 105 (2009).
[28] R.E. Taylor, Thermal Expansion of Solids, Asm Intl, 1998.
[29] D.N. Talwar, J.C. Sherbondy, Appl. Phys. Lett. 67 (1995) 3301-3303.
[30] S.R. Nishitani, R. Takeda, H. Ishii, Y. Yamamoto, T. Kaneko, J. Japan Inst. Metals 73 (2009) 566-570.
[31] S. Limpijumnong, W.R.L. Lambrecht, Phys. Rev. B 57 (1998) 12017-12022.
[32] M.J. Rutter, V. Heine, J. Phys.: Cond. Matt. 9 (1997) 8213.
[33] E. Konstantinova, M.J.V. Bell, V. Anjos, Intermetallics 16 (2008) 1040-1042.
[34] R. Hill, Proc. Phys. Soc. London Sec. A 65 (1952) 349-355.
[35] R.G. Munro, J. Phys. Chem. Ref. Data 26 (1997) 1195-1203.

[36] Z. Li, R.C. Bradt, J. Mat. Sci. 22 (1987) 2557-2559.
[37] Z. Li, R.C. Bradt, Intl. J. Hi. Tech. Ceram. 4 (1988) 1.
[38] M.E. Straumanis, S. Zyszczynski, Journal of Applied Crystallography 3 (1970) 1-6.